Revisiting the Band Gap problem in bulk Co_3O_4 and its isostructural Zn and Al derivatives through the lens of theoretical spectroscopy

Anneke Dittmer,[1] Tiago Leyser da Costa Gouveia,[1] Kantharuban Sivalingam,[1] Serena DeBeer,[*2] Frank Neese,[*1] and Dimitrios Maganas[*1]

Supplementary Information

Table of Contents

1 Supplementary material for experimental studies from literature

Table S1. Overview of experiments from literature.

Reference	Material	Measurement	Wavelength range / eV	Absorption Bands/ eV	Assignment Absorption Bands	Band Gaps / eV	Assignment Band Gaps	Method
Cherkashin, 1969[1]	Ceramic	UV/Vis Spectrometer	-	0.81 1.50	-	-	-	-
Tanaka, 1979[2]	Polycrystalline sample, Ceramic	UV/Vis Spectrometer (self-build in lab)	1.0-3.5	1.7 3.1	-	-	-	-
Belova, 1983[3]	0.1-0.5 µm Thin Film	Opt. Transmission Spectra (UV/Vis/NIR), Perkin-Elmer-spectrometer 450	0.5-6.1	0.87 1.70 2.85 5.39	e(Co(II)) -> t2(Co(II)) e(Co(II) -> 4s(Co(II)) t2g(Co(III)) -> eg(Co(III)) 2p(O) -> 4s(Co(III)) *Characterization based on SCF XaSW, Tanabe-Sugano	-	-	-
Martens, 1985[4]	Ceramic: Pellets from powder (hot pressed)	Ellipsometer	0.7-5.5	0.80 1.60 2.65 4.40	Origin uncertain Transitions related to Co(III) *assigned due to substitution with Co in $CoFe_2O_4$	-	-	-
Cook, 1986[5]	Thin Film (polycrystalline)	opt. Transmission (T) Cary-17, Ellipsometer (E) (300-1000n)	0.5-4.1	0.82 (T) 0.93 (T) 1.7 (T)/1.6 (E) 2.8 (T)/2.7 E)	e(Co(II)) -> t2(Co(II)) e(Co(II)) -> eg(Co(III)) t2g(Co(III)) -> t2(Co(II)) 2p(O) -> t2(Co(II)) *assigned based on Miedzinska	-	-	-
Murad, 1988[6]	0.1-0.2 µm Thin Film (spray pyrolysis)	Pye-Unciam SP8-100 spectrophotomer	1.4-4.1	-	-	1.45 2.00 3.20	3x direct allowed BGs	Tauc relation
Schumacher, 1990[7]	0.1 µm Thin Film (sputtering)	Photorepsonse	1.5-4.1	-	-	1.5	Indirect BG (1A1->1T1 Oh Co3+) *based on Martens	Tauc relation from quantum efficiency data
Varkey, 1993[8]	0.02-0.1 µm Thin Film	Philips PU 3700 spectrophotometer	1.4-4.1	-	-	1.65	Optical BG	Extrapolated linear portion
Lenglet, 1994[9]	Thin Film (decomposition (D) of cobaltous nitrate vs. sol gel method (S))	Optical Spectra	0.5>	0.85 (D)/0.84 (S) 0.95/0.93 1.85/1.85 3.45/3.35 4.80/4.70	-	-	-	-
Nkeng, 1995[10]	0.01-2 µm Thin Film (sputtering (SU) vs. spray pyrolysis (SY))	UV/Vis/NIR reflectance spectroscopy (Lambda 9 Perkin-Elmer spectrometer)	0.5-6.2	0.82(SU)/0.84(SY) 0.93/0.95 1.70/1.95 2.80/3.55	-	-	-	-

Patil, 1996[11]	1.9 µm Thin Film (spray pyrolysis)	Hitachi 330 spectrophotometer	1.5-3.5	0.48 1.02 1.08 1.12 1.26 1.38	-	0.75 1.10 1.26 1.38 1.44 2.06	Indirect forbidden opt. BG Indirect allow. opt. BG Direct forbidden opt BG Direct forbidden opt BG Direct allow. opt BG Direct allow. opt BG	Tauc relation
Ruzakowski Athey, 1996[12]	0.015-0.022 µm Thin Film (Spray Pyrolysis)	Transmittance/ Ellipsometry J.A. Woollam Co., Inc. Rotating analyzer VASE	0.7-3.5	0.83 0.94 1.70 2.90	e(Co(II)) -> t2(Co(II)) e(Co(II)) -> eg(Co(III)) t2g(Co(III)) -> t2(Co(II)) 2p(O) -> t2(Co(II)) * assigned based on Miedzinska	-	-	-
Cheng, 1998[13]	0.65 µm polycrystalline thin Film (CVD)	Shimazu spectrophotometer UV-140, Transmission	1.3-2.2	1.6-1.7 2.8-2.9	- LMCT	1.50-1.52 1.88-1.95	2x direct allow. opt. BGs Co(III)-Co(II) O-Co(II)	Tauc relation
Barreca, 2001[14]	0.204-1.276 µm Thin Film (CVD)	Opt Abs UV-VIS-NIR dual beam spectrophotometer: Carry 5E (Varian)	0.6-4.1	0.82 0.98 1.70 2.48	e(Co(II)) -> t2(Co(II)) e(Co(II)) -> eg(Co(III)) 2p(O) -> eg(Co(III)) 2p(O) -> t2(Co(II)) *assigned based on Nkeng, Belova, Cook	1.5 2.0	Subband inside 'true' opt. BG, O 2p->Co(III) 3d 'true' opt. BG, interband transitions (O 2p->Co(II) 3d)	Tauc relation
Kadam, 2001[15]	0.9(A)-1.7(B) µm Thin Film (PSPT)	Hitachi model-330 spectrophotometer	1.5-3.5	1.04 (A)/0.88 (B) 1.16 (A)/1.08 (B)	-	1.10(A)/0.98(B) 1.46(A)/1.42(B) 2.10(A)/2.02(B)	Indirect allow. opt. BG 2x direct allow. opt. BGs	Tauc relation
Pejova, 2001[16]	0.6 µm Thin Film (polycrystalline)	Hewlett Packard 8452A spectropho-tometer (UV-vis spectral region)	1.5-4.0	-	-	2.2	Direct allow. opt. BG	Tauc relation
Kim, 2003[17]	1.0 µm Thin Film (sol-gel method)	Elipsometry (rottating analyzer)	1.5-4.0	1.65 2.40 2.80	t2g(Co(III)) -> t2(Co(II)) 2p(O) -> eg(Co(II)) 2p(O) -> t2(Co(III)) * assigned based on Miedzinska	-	-	-
Mane, 2003[18]	Thin Film (MOCVD)	UV/Vis Spectrophotometry (Hitachi UV-visible Spectrophotometer model U-300)	1.4-3.1	-	-	1.45 2.05	2x direct allow. opt. BG	Tauc relation
Gulino, 2003[19]	Thin Film (MOCVD)	UV/Vis Spectrometer (Beckman DU650)	1.2-3.5	-	-	1.48 2.19	2x direct allow. opt. BG	Tauc relation
Yamamoto, 2003[20]	0.0068/0.0136 µm Thin Film (sol-gel method)	opt spectrum analyzer Hitachi Ltd., U-3500, IR optical spectrum analyzer (Ando Electric Co. Ltd., AQ 6315A) with white light (Ando Electric Co. Ltd., AQ 4303B)	0.5-3.5	0.75 0.90 1.70 3.00	-	0.80 (0.7 & 1.0) 1.30 2.10	e(Co(II)) -> t2(Co(II)) t2g(Co(III)) -> t2(Co(II)) 2p(O) -> t2(Co(II)) *assigned based on Miedzinska all three: direct allowed opt. BGs	Tauc relation
Bahlawane, 2004[21]	0.03-0.04 µm Thin Film (CVD)	UV–Vis spectrometer, UVIKON 860, KONTRON Instruments	1.5-4.1	1.69 3.02	-	1.43 2.15	t2g(Co(III)) -> t2(Co(II)) 2p(O) -> t2(Co(II)) *assigned based on Miedzinska both: direct allowed opt. BGs	Tauc relation

Shinde, 2006[22]	0.8 µm Thin Film (Spray Pyrolysis)	Systonic Spectrophotometer-119	1.2-3.5	-	-	1.6 2.1	Indirect allow. opt. BG Direct allow. opt. BG	Tauc relation
Thota, 2009[23]	powder (nanocrystaline, sol-gel method)	UV-vis-NIR spectrophotometer (Varian based Cary 5000)	0.6-6.2	0.56 0.85 0.95 1.77 3.12	e(Co(II)) -> t2(Co(II)) e(Co(II)) -> t2(Co(II)) e(Co(II)) -> eg(Co(III)) t2g(Co(III)) -> t2(Co(II)) 2p(O) -> t2(Co(III)) *assigned based on Lenglet, Kim, XRD	1.52 2.53	Opt. BG (subband located in energy gap), O->Co(II) Opt. BG, O->Co(III)	Tauc relation
Ngamou, 2010[24]	0.325 µm Thin Film (CVD)	Shimadzu UV-vis spectrophotometer	1.4-3.1	-	-	1.52 2.14	O->Co(III) O->Co(II)	Tauc relation
Louradi, 2011[25]	0.4-0.5 µm Thin Film (spray pyrolysis, T=300°C-500°C)	SHIMADZU 3101 PC UV-VIS-NIR spectrophotometer	0.5-4.1	-	-	1.48/1.51 2.08/2.11	T=300°C/T=500°C All: direct BGs	Tauc relation
Qiao, 2013[26]	0.017 µm Thin Film	optical absorption, Phioluminesence (PL)	0.5-6.2	0.7 1.6 2.2 (3.7) 4.4	Lowest energy band has three peaks (0.7-1.1 eV) DFT assigned	0.76 /0.74 (PL) 1.60	Fundamental BGs	Tauc relation
Waegle, 2014[27]	0.01-0.06 µm Thin Film (magnetron sputtering)	Shimadzu UV-2600 spectrohphotometer (Shimadzu Scientific Instruments, Columbia, MD)/ FT-IR Bruker Vertex 70V (Bruker optics, Billerica, MA)	0.7-3.0	0.82 0.94 1.66 2.84	e(Co(II)) -> t2(Co(II)) e(Co(II)) -> eg(Co(III)) t2g(Co(III)) -> t2(Co(II)) 2p(O) -> t2(Co(III)) *Miedzinska mentioned	(0.7) 1.6	Midgap (d-d transition, not named BG) BG	Beer's Law
Jiang, 2014[28]	0.01 µm Thin Film	UV/Vis-NIR	0.6-3.5	0.82 0.93 1.64 2.81	*based on XUV? (Extreme UV) Pathways 3.0 eV: 2p(O) -> eg2(Co(III))	1.6	Direct BG	-
Reddy, 2017[29]	Thin Film (sputtering)	UV-vis: Shimadzu UV-3600 plus UV-vis-NIR spectrophotometer	1.0-4.1	-	-	1.4	BG	From UV/Vis (no further specification)
Lakehal, 2018[30]	0.256 µm Thin Film (deposited, sol gel method)	Shimadzu-1650 spectrophotometer	1.4-4.1	-	-	1.5 2.2	2p(O) -> eg(Co(III)) 2p(O) -> t2(Co(II)) *assigned based on Lit 19-22 both: direct allowed opt. BGs	Tauc relation
Zhang, 2020[31]	0.15-0.18 µm Thin Film	Optical Transimission Spectra	0.6-4.1	-	-	1.5	Direct fundamental opt. BG	Tauc Plot

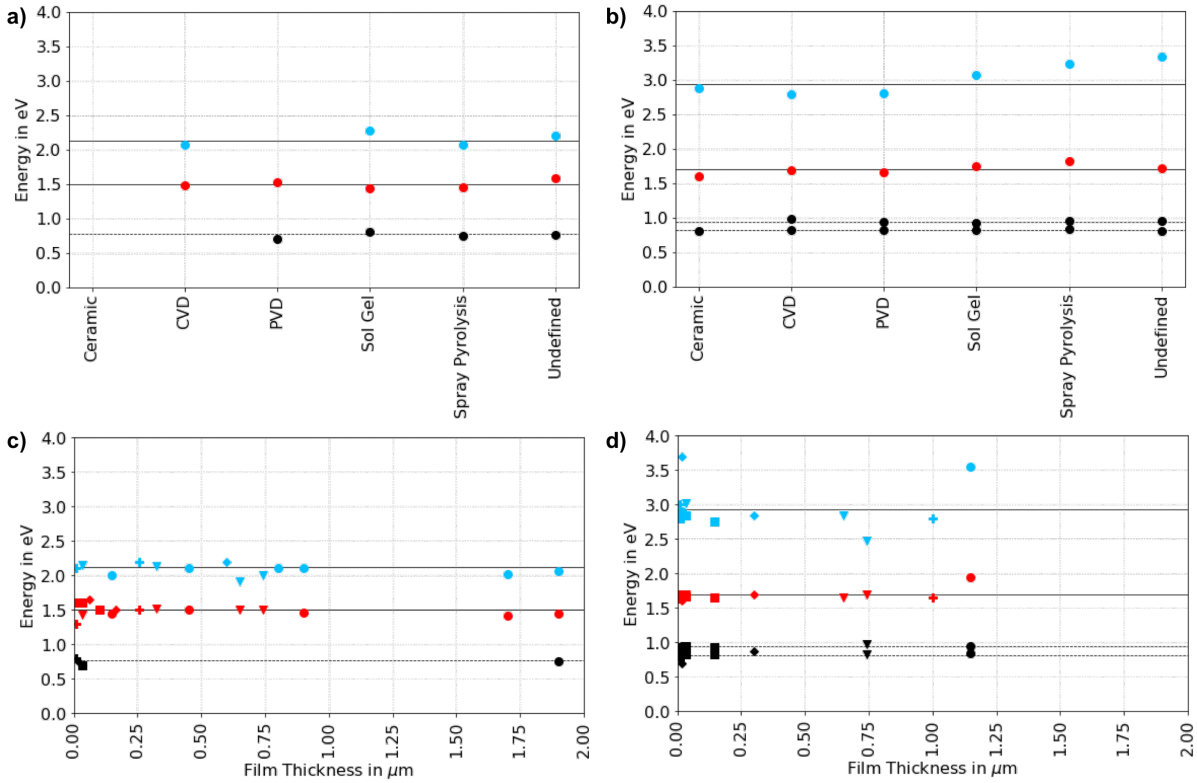

Figure S1. Relation between method to prepare Co_3O_4 sample and experimental **a)** band gaps and **b)** absorption bands as well as relation between film thickness of Co_3O_4 thin films for **c)** band gaps and **d)** absorption bands with triangles symbolizing CVD, squares PVD, pluses sol gel, circles spray pyrolysis, and diamonds undefined prepared thin films

2 Supplementary material for computational studies from literature

Table S2. Overview of calculations from literature

Reference	Model	Method	Band Gaps / Excitation Energies / eV	BG type/ transition character	Other Information
Belova, 1983[3]	• $[CoO_4]^{6-}$ & $[CoO_6]^{9-}$ cluster in electrostatic model • electrostatic model: average external field parameters determined by XPS data • "Watson spheres"	• SCF-XαSW (self-consistent field Xα (α = exchange parameter) scattered wave cluster method, spin restricted calculation • Orbital difference • Spin polarized considerations derived from results of method above	0.80 2.18 2.61 5.67 6.39 0.87 1.38 2.18 2.61 5.67	Co(II) e→t_2 Co(II) e→4s Co(III) t_{2g}→e_g O 2p→Co(II) 4s O 2p→Co(III) 4s Co(III) $e_g^{\alpha\backslash} rightarrow t_{2g}$ Co(II) t_2^{α}4s Co(II) e→4s Co(III) $e_g^{\alpha\backslash} rightarrow e_g$ O 2p→Co(II) 4s	Co(III) might be HS due to symmetry lowering
Miedzinska, 1987[32]	• Unit cell	• Semi-empirical form of MOs, VS1E, Wolfberg-Helmhotz approximation • Energies of separated atom orbitals determined first, then interaction energies of overlapping orbitals • Resulting energy differences assigned to observed spectroscopic transitions • 1. Orbital energies of isolated gas phase ions are from empirical ionization potentials • 2. Geometry of the ion in lattice is recognized and the orbitals split if necessary into sets of lower degeneracies • 3. Orbital VS1E values are adjusted for Pauling electroneutrality effect permitting partial reduction of ions (Co(II/III) and O(-II)) • energy level diagram via Wolfgang-Helmholtz approximation for $[Co^{2+}O^{2-}{}_4]$ and $[Co^{3+}O^{2-}{}_6]$ • 6x $[Co^{2+}O^{2-}{}_4]$ with one center $[Co^{3+}O^{2-}{}_6]$, orbitals of 6 units Co(II) are linear combined to give group orbitals of ligands, overlap Co(III) orbitals	0.8 1.0 1.3 2.1	Co(II) e→t_2 Co(II) t_2→Co(III) e Co(III) t_{2g}→Co(II) t_2 O 2p→Co(II) t_2	Distortion removes orbital degeneracies
Wang, 2006[33]	• Periodic Boundary Conditions	• VASP • PAW • Energy cut-off: 550 eV • Spin-polarized • GGA • GGA+U = 3.3 eV	0.7 1.6	GGA GGA+U	GGA: 2.39 μ_B GGA+U: 2.67 μ_B

Walsh, 2007[34]	• Co-Fe-Al oxide spinel systems • Periodic boundary conditions • 14 atom primitive spinel unit cell • special quasirandom structure (SQS) model used for random occupation in inverse structure	• VASP • Plane wave function set with 500 eV upper energy threshold • 6x6x6 k-point grid for Brillouin zone • projecter augmented wave method used to represent valence-core interactions • spin polarized • scalar relativistic approximation • Gradient corrected DFT with the Co & Fe 3d (3d robtials highly correlated -> U necessary) states treated with on-site correction for Coulomb interaction (DFT+U) • PBE+U • U tested from 2 to 5 eV -> electronic structure quite independent, U=2 eV for Co 3d and U=3 eV for Fe 3d chosen because BGs in region of experimental data • BG from difference in DOS	Co_3O_4 1.23 1.51 1.67 Al_2CoO_4 2.32 2.61 2.65	Co_3O_4 X-X Direct trans. Γ-X indirect trans. Γ- Γ Direct trans. Al_2CoO_4 Direct transition Indirect transition Direct transition Called Electronic BG VBM = mixture of states td Co 3d and O 2p CBM = oh Co 3d	• Electronic BG of Co_3O_4 and Fe_3O_4 do not change significantly if tetrahedral sites are replaced (M_2AlO_4 – inverse spinel) but increase greater than 1 eV if octahedral sites are replaced (MAl_2O_4 – normal spinel) • Co Al_2O_4 seems to be most suitable for PEC catalysis • **Magnetic moments available**
Xu, 2009[35]	• Periodic boundary conditions	• DMol[3] program package in Materials Studio of Accerys Inc. • PBE • Double-numerical basis with polarization functions (DNP) • For O Atoms all electron basis sets, for Co cores with ECPs • Fermi smearing of 0.01 Hartree, cutoff energy 4.5 Å • SCF convergence 10^{-6} Hartree • Optimized geometry • Spin-polarized approach • Brillouin zone 5x5x5 Monkhorst-Pack grids for bulk (k points)	1.75 (↑) 1.92 (↑) 2.06 (↑) 2.2 (↓) 2.9 (↓) 3.3 PBE 0.30 0.75 0.94 1.39	X-X Direct gap, O 2p→Co(II) t_{2g} Γ-X Indirect gap Γ- Γ Direct gap, Co(III) t_{2g}→Co(II) t_{2g} O 2p→Co(II) t_{2g} O 2p→Co(III) e_g Co(III) t_{2g}→Co(II) t_{2g} PBE X - X Direct BG Γ - X Indirect BG X – Γ Indirect BG Γ - Γ Direct BG	• bulk shows antiferromagnetic properties • Antiferromagnetic (Co(II) = 2.631μ_B • Experimental value Co(II) = 3.26 μ_B • Strong hybridization of the Co^{3+} 3d states with O 2p states
Chen, 2011[36]	• Periodic boundary conditions • 14-atom primitive unit cell of spinel structure • conventional cubic cell with 56 atoms and tetragonal supercell containing 112 atoms considered	• Quantum Espresso package: DFT-GGA and GGA+U • Spin-polarized • PBE • Norm conserving Troullier-Martins pseudopotantials • Plane-wave kinetic energy cutoff = 120 Ry • 8x8x8 k-point grid convcerged sampling of Brillouin zone • U(Co(II)) = 4.4 eV • U(Co(III)) = 6.7 eV • PBE0: localized Wannier orbitals obtained through a unitary transformation of delocalized Bloch states corresponding to occupied bands, maximal localized Wannier functions (MLWFs)	PBE+U 1.96 2.41 2.81 3.25 1.67 2.02 2.16 PBE0 3.42	PBE+U (4.4/6.7) X - X Direct BG Γ - X Indirect BG X – Γ Indirect BG Γ - Γ Direct BG PBE+U=4.4 PBE+U=5.9 PBE+U=6.7 PBE0 Minimum BG	• Valence Band two subbands: lower energies dominated by O 2p and upper by Co3+ d, smaller amounts of Co2+ present as well • Bottom of conduction band: Co2+ and Co3+ 3d • Co(II),PBE = 2.64 μ_B/ J1=-2.5x10-3 • Co(II),PBE+U = 2.84 μ_B/ J1=1.0x10-4 • Co(II),PBE0 = 2.90 μ_B/ J1=-5.0x10-3 • Exp = = 3.26 μ_B/ J1=-6.26x10-4

Montoya, 2011[37]	• Periodic ab-initio	• VASP • PAW • Plane-wave expansion truncated cut-off energy of 550 eV • BZ integration: 6x6x6 Monkhorst-Pack k-points grid • PBE • PBE+U = 3.3 eV	0.1 1.6	PBE PBE+U	• PBE+U: 1.6 μ_B
Qiao, 2013[26]	• Periodic boundary conditions (?)	• DFT and DFT+U tested • DFT without U gives best structure • DOS • Orbital difference • Oscillator strength (p-d magnitudes stronger than d-d) • U distorts band structure	0.83 0.95 1.04 1.64 1.84 2.62 3.66 4.69 5.8	Direct tranistions (first is BG) Co(II) e_g→Co(II) t_{2g}(↓) Co(II) e_g→Co(III) e_g(↓) Co(II) e_g→Co(III) e_g(↑) Co(III) t_{2g}→Co(II) t_{2g}(↓) Co(III) t_{2g}→Co(III) e_g O 2p(I)→Co(II) t_{2g}(↓) O 2p(I) →Co(III) e_g O 2p(II) →Co(II) t_{2g}(↓) O 2p(II) → Co(III) e_g	• CoO a classic highly correlated Mott insulator • Co3O4 did not exhibit such strong electron correlations and its electronic structure can be well described by standard DFT • First five transitions are pure d-d type tranistions either inside a homovalent Co ion or between two heterovalent Co ions depending on the spin orientation • d-d transitions would be nominally forbidden for non-hybridized d bands. However, a non-zero transition matrix element between the initial and final states may result from hybridization of the O 2p and Co 3d orbitals, which will lightly relax the parity selection rule and result in a non-zero transition probability • lifetime broadening of the electron–hole pairs
Lima, 2014[38]	• Periodic boundary conditions	• WIEN2k • Full-potential linear augmented plane wave (FP-LAPW) method • Plane waves limited by cut-off at K_{max}=8.0/R_{MT} • Charge density was Fourier-expanded up to G_{max}=14 • k-point grid: 8x8x8 well converged sampling of Brillouin zone • GGA-PBE • mBJ (semilocal potential) • B3PW91 • Optimized structure • TDOS, PDOS (total and partial electronic density of states) • Absorption curve: electric-dipole allowed transitions from the populated Kohn-Sham states	GGA-PBE 0.35 0.80 0.95 1.35 mBJ 2.84 3.00 3.20 3.40 B3PW91	GGA-PBE X - X Direct BG Γ - X Indirect BG X – Γ Indirect BG Γ - Γ Direct BG mBJ X - X Direct BG Γ - X Indirect BG X – Γ Indirect BG Γ - Γ Direct BG B3PW91	• Dominated by: Co(II) e_g→Co(II) t_{2g} and Co(III) t_{2g}→Co(III) e_g • Superposition of both optical transitions • Consequently, the calculations predict that the crystal field splitting at both sides are of the same magnitude

			1.55	X - X Direct BG	
			2.00	Γ - X Indirect BG	
			2.40	X – Γ Indirect BG	
			2.80	Γ - Γ Direct BG	
			1.86, 2.4, 2.9 (Abs peaks)	Dominated by $Co(II)\ e_g \rightarrow Co(II)\ t_{2g}$ And $Co(III)\ t_{2g} \rightarrow Co(III)\ e_g$	

Singh, 2015[39]	• Periodic boundary conditions	**DFT:**
		• VASP
		• PBE
		• PBE+U
		• HSE06 (range-separated exchange-correlation functional)
		• Valence electrons described by Kohn-Sham single-electron orbitals
		• Plane-wave bases with an energy cut-off of 500 eV
		• Core electrons were defined within PAW methodology
		• PBE & PBE+U: k point grid 8x8x8
		• BZ integration done with tetrahedron method with Blöchl corrections
		• HSE06: k point grid 4x4x4
		• BZ: integrated using Gaussian smearing with smearing width 0.01 eV
		• U(Co(II) = 4.4 eV
		• U(Co(III)) = 6.4 eV
		• HSE06: HF exchange 25%, 20%, 17%, 15%, 13%, 10%, 5%
		• Investigation between fundamental and optical band gap: dielectric tensor calculated in PAW framework
		• COHPs (crystal orbital Hamiltonian populations) – LOBSTER program
		Many-body Green's function (GW)
		• GW approximation requires input of initial-guess quasiparticle energies and wave functions which are usually taken from KS-DFT
		• 'perturbation theory improvement to DFT'
		• G0W0: perturbative non-self-consistent GW method
		• GW: self-consistent GW approach
		• QSGW: quasiparticle self-consistent GW
		  ○ Sc-GW0: QP eigenvalues & WF both updated in G
		  ○ Sc-GW: QP eigenvalues & WF both updated in G & W
		• Input WF & energies for G0W0 obtained from DFT calc. on bulk unit cell using PBE, PBE+U, HSE06 (5%)
		• :G0W0: k point grid 4x4x4
				Direct BG	• linear dependency of BG on HF exchange
					• **magnetic moments available**

			0.34	PBE	
			2.45	PBE+U	
			0.78	HSE06 (5%)	
			0.79	Sc-GW0	
				Indirect BG	
			0.82	GW0	
			0.94	GW	
			0.98	G0W0	
			0.98	Sc-GW	

		• q point mesh of response function: 2x2x2 •			
Kaptagay, 2015[40]	• periodic slab model (infinite in two dimensions) • bulk contains 2 formula unites, i.e. 14 ions	• VASP • PAW • PBE+U(=3 eV) • Standard Monkhorst-Pack grid 4x4x4 k point sampling mesh for bulk • Cut-off energy 600 eV • Methfessel-Paxton smearing with 0.1 eV	1.60	Band gap	• Magnetic moment Co(II) 2.63 μ_B
Lima, 2016[41]	• Periodic boundary conditions • Normal spinel structure	• WIEN2k • FP-LAPW • With and without SOC • PBE • PBE+U • B3PW91 • K points: 8x8x8 • SOC via second-variation procedure using scalar relativistic eigenfunctions	wo/wSOC 0.72/0.86 1.11/1.26 1.34/1.50 1.49/1.66 1.86/2.04 1.60/1.65 2.04/2.12 2.42/2.48	Wo/wSOC B3PW91 (α=5%) B3PW91 (α=10%) B3PW91 (α=13%) B3PW91 (α=15%) B3PW91 (α=20%) PBE+U=3.0/3.0 Co(2/3) PBE+U=4.4/4.4 PBE+U=4.4/6.7	Wo/wSOC 2.33/2.33 μ_B J1= -3.2/-2.8 μ eV 2.40/2.40 μ_B J1= -5.3/-3.5 μ eV 2.43/2.43 μ_B J1= -6.5/-6.3 μ eV 2.45/2.45 μ_B J1= -7.3/-7.6 μ eV 2.49/2.49 μ_B J1= -11.8/-11.2 μ eV 2.35/2.36 μ_B J1= -0.3/-1.8 μ eV 2.40/2.38 μ_B J1= -1.9/-0.5 μ eV 2.42/2.42 μ_B J1= -1.1/-4.3 μ eV AFM always more favourable not influence by U or α or SOC
Zaki, 2018[42]	• Periodic Boundary Conditions	• CASTEP program package in Material Studio of Accelrys Inc • PBE+U = 3.5 eV (GGA-PBEsol+U) • Plane wave basis with kinetic energy cut-off of 380 eV • Monkhorst-Pack grid 6x6x6 k-points • PDOS	1.26 1.77 1.61 2.22	X - X Direct BG Γ - X Indirect BG X – Γ Indirect BG Γ - Γ Direct BG	• Dielectric function available

Sousa, 2019[43]	• Periodic Boundary Conditions	• WIEN2k • PBE • Becke-Johnson XC • FP-LAPW (full potential augmented plane wave) • $K_{max} = 8 / R_{MT}(O)$ • K point grid: 8x8x8 • Charge density foruier expanded Gmax = 12 • SIESTA: magnetic properties under pressure • Basis et: finite range pseudoatomic orbitals (PAO's) of Sankey-Nicklewsky • Double-zeta Plus Ploarization (DZP)	0.35 0.06 1.33 0.96 2.60	PBE LDA B3PW91 BJ mBJ	2.20 μ_B 1.94 μ_B 2.42 μ_B 2.26 μ_B 2.62 μ_B
Zhandun, 2020[44]	• Periodic Boundary Conditions	• VASP • PAW • PBE • PBE+U=4.5 eV • G0W0 • Cut-off energy 500 eV • 8x8x8 Monkhorst-Pack mesh of k points	0.2 0.35 0.6	PBE PBE+U G0W0	•
Cadi-Essadek, 2021[45]	• Periodic Boundary Conditions	• VASP • PAW • PBE • Long-range dispersion interaction DFT-D3 • PBE+U • 8x8x8 k point mesh	0.35 0.55 0.75 0.98 1.21 1.43 1.64 1.86 2.07 2.28 2.46	PBE+U=0.0 PBE+U=0.5 PBE+U=1.0 PBE+U=1.5 PBE+U=2.0 PBE+U=2.5 PBE+U=3.0 PBE+U=3.5 PBE+U=4.0 PBE+U=4.5 PBE+U=5.0	2.27 μ_B 2.36 μ_B 2.43 μ_B 2.49 μ_B 2.53 μ_B 2.58 μ_B 2.61 μ_B 2.65 μ_B 2.68 μ_B 2.71 μ_B 2.73μ_B

2.1 Summary of computational studies

Besides the consulted experimental investigations, multiple published computational studies investigated the magnitude and nature of the different candidate band gaps in Co_3O_4. Figure S2,[33, 36, 37, 39-41, 43-45] Figure S3,[34-36, 38, 42] and Table S3[3, 26, 32, 35, 38] summarize a selection of these studies. Table S2 provides further details on all references. An outline concerning noteworthy outcomes from all these studies is provided below.

2.1.1 Summary of computational studies targeting a selected band gap with different methods

Figure S2 summarizes literature references targeting one selected band gap using different DFT methods with periodic boundary conditions. Most of these calculations[33, 36, 37, 40, 43-45] focus on the experimental band gap at 1.51 eV, based on the works of Shinde et al.[22] and Kim et al.[46] Some calculations[41] target the band gap at 2.14 eV, while others[38, 39, 44] consider the experiment of Qiao et al.[26] and its band gap value of 0.74 eV.

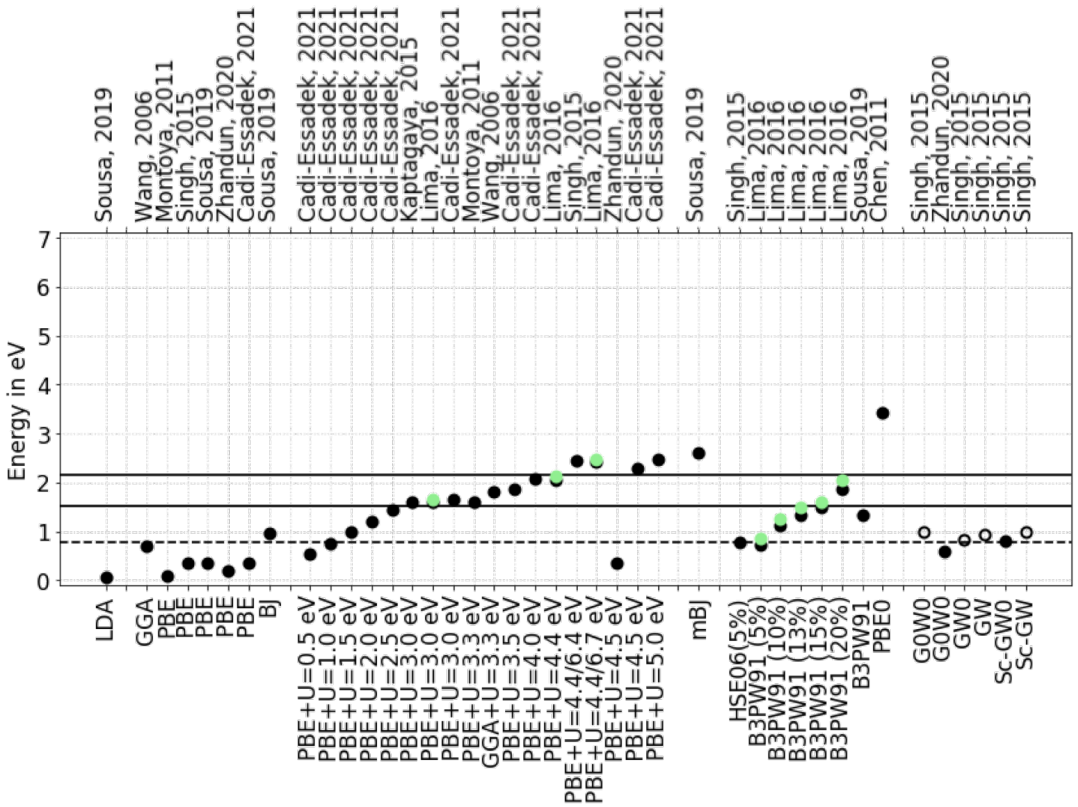

Figure S2. Overview on calculated band gaps found in literature.[33, 36, 37, 39-41, 43-45] Unfilled circles: indirect band gaps. Filled circles: direct band gaps. Green circles: Band gap including SOC.

Most studies of the band gap of Co_3O_4 use GGA functionals, most commonly PBE.[37, 39-41, 43-45] GGA functionals are known to underestimate the experimental band gap.[47] In many cases, the calculated band gap is close to zero.[37, 39, 43-45] To overcome this problem, the effective on-side potential U (DFT+U) is often used to adjust the calculated band gap energies towards the experimental value. This approach is commonly used for highly correlated materials such as Co_3O_4.[39]

Studies such as Cadi-Essadek et al.[45] have shown that applying an effective on-site potential U can adjust the calculated band gap energies of Co_3O_4 towards the experimental value, with the band gap increasing linearly with increasing U. Various approaches, such as using different values of U for Co(II) and Co(III), have been explored.[36, 39] While this method is efficient in obtaining the desired band gap value, it can also lead to undesirable modifications in the electronic structure of the system.[39]

Lima et al.[41] found that the band gap calculated with hybrid functionals has a linear relationship with the percentage of Hartree-Fock exchange, similar to GGA+U, but without altering the electronic structure. They also observed a slight increase in the band gap after incorporating spin-orbit coupling. Singh et al.[39] and Zhandun et al.[44] used Green's Function methods to study the band gap, and their results agree with the first band gap at about 0.78 eV. While all DFT methods in Figure S2 predict a direct band gap, Green Function approaches produce ambiguous results with indirect or direct character.

To determine the band gap and its character, most of the described studies use density of states (DOS) calculations, where the band gap is defined as the difference between the valence band maximum and the conduction band minimum. However, without considering the exciton binding, this approach provides only the fundamental band gap, not the optical one. Nevertheless, this method is valid for (meta-)GGA functionals because they lack XC energy, resulting in the same fundamental and optical band gap as previously studied.[48]

2.1.2 Summary of computational studies targeting multiple band gaps with different methods

The studies[34-36, 38, 42] summarized in Figure S3 have identified more than one band gap by periodic calculations aimed in particular at the experimental band gaps at 1.51 eV and 2.14 eV.

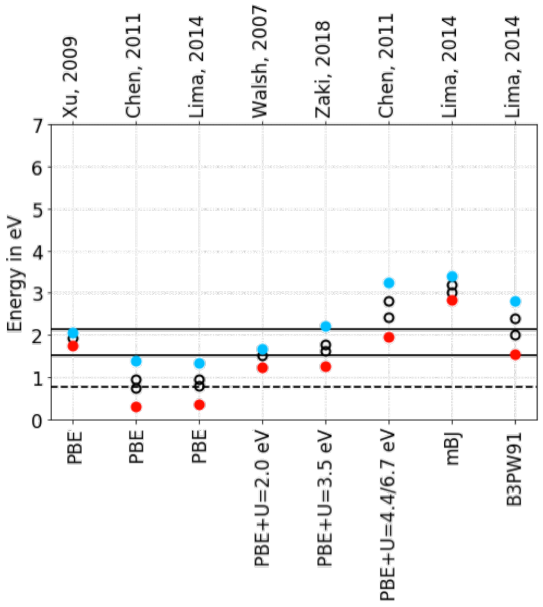

Figure S3. Overview on calculated band gaps found in literature including more than one band gap.[34-36, 38, 42 33, 36, 37, 39-41, 43-45] Unfilled circles: indirect band gaps. Filled circles: direct band gaps.

In all cases two direct band gaps have been calculated. In addition, one or two indirect band gaps were identified between the two direct band gaps. The lower direct band gap has the character X→X, while the higher one has the character Γ → Γ where X and Γ describe different high symmetry points in the Brillouin zone. The indirect band gaps have X→ Γ and Γ→X characters. As with the previously discussed results involving only one band gap, there is no general consistency in the resulting band gap values.

2.1.3 Summary of computational studies characterizing absorption bands and band gaps

Various studies discussed the transition character of the absorption bands and band gaps in the orbital picture. Table S3 summarizes a selection of studies.[3, 26, 32, 35, 38]

Table S3. Transition character based on calculations. Transition energy in eV.

	Belova, 1983[3]	**Belova, 1983[3] (spin)**	**Miedzinska, 1987[32]**	**Xu, 2009[35]**	**Qiao, 2013[26]**	**Lima, 2014[38]**
Method	SCF-XαSW, spin restricted	Data reconsidered with spin	Semiempirical MO (VS1E)	PBE/DNP, spin polarized	DFT (GGA)	B3PW91/FP-LAPW, dielectric function
Model	$[CoO_4]^{6-}$ & $[CoO_6]^{9-}$ cluster in electrostatic model (external field)		Unit Cell	Periodic	Periodic	Periodic
Co(II) e→t_2	0.80	-	0.8	-	0.83 (↓)	1.86/2.4/2.9
Co(III) t_{2g}→e_g	2.61	0.87	-	-	1.84	1.86/2.4/2.9
Co(III) e_g →e_g	-	2.61	-	-	-	-
Co(II) t_2→Co(III) e_g	-	-	1.0	-	0.95(↓)/1.04(↑)	-
Co(III) t_{2g}→Co(II) t_2	-	-	1.3	(2.06(↑)/)3.3(↓)	1.64	-
O 2p→Co(II) t_2	-	-	2.1	(1.75(↑)/)2.2(↓)	2.62(↓)/4.69(↓)	-
O 2p→ Co(III) e_g	-	-	-	2.9 (↓)	3.66/5.80	-
Co(II) e→4s	2.18	1.38	-	-	-	-
Co(III) t_{2g}→4s	-	-	-	-	-	-
O 2p→Co(II) 4s	5.67	5.67	-	-	-	-
O 2p→Co(III) 4s	6.39	-	-	-	-	-

Xu et al.[35] have assigned the X→X transition to the LMCT orbital transition, O 2p→Co(II) t_{2g}, and Γ → Γ to Co(III) t_{2g}→Co(II) t_2, resulting in band gaps of 1.75 eV and 2.06 eV, respectively.

Miedzinska et al.[49] identified a transition at 1.30 eV as MMCT Co(III) t_{2g}→Co(II) t_2, while the next higher transition at 2.10 eV was assigned to LMCT O 2p→Co(II) t_{2g}. Two additional transitions were identified at 1.0 eV as MMCT Co(II) t_2→Co(III) e_g and at 0.8 eV as a ligand field transition Co(II) e→t_2. The results presented in Miedzinska et al. [49] were obtained using a semiempirical MO method with a unit-cell model and not with periodic boundary conditions, unlike the more recent studies.

Belova et al.[3] also observed the ligand field transition Co(II) e→t_2 at an energy of 0.80 eV. They used an SCF-XαSW approach with isolated $[Co(II)O_4]^{6-}$ and $[Co(III)O_6]^{9-}$ clusters in an external electrostatic field. A more recent study by Qiao et al.[26] utilizing DFT (GGA) with periodic boundary

conditions also located the same transition at a similar energy of 0.83 eV and assigned it as the band gap.

The sequence of transitions presented in the periodic DFT study by Qiao et al.[26] agreed reasonably well with the earlier study of Miedzinska et al.[49]. Qiao et al.[26] predicted an MMCT Co(II) t_2→Co(III) e_g transition at 0.95 eV, followed by Co(III) t_{2g}→Co(II) t_2 at 1.64 eV, the ligand field transition of Co(III) at 1.84 eV, and finally the LMCT O 2p→Co transitions of Co(II) and Co(III) at 2.62 eV and 3.66 eV, respectively. The intensity of the transitions increased with increasing excitation energy, except for the ligand field transition of Co(II), which had a higher intensity than the MMCT Co(II) t_2→ Co(III) e_g.

The established transition characters have been challenged by Lima et al.[38]. They argue that the MMCT transitions are unlikely to occur at energies as low as the band gap values. They also made a similar claim for the LMCT transitions. Their absorption spectrum was calculated using the dielectric function based on DOS results obtained with the hybrid functional B3PW91 and periodic boundary conditions. They identified the resulting absorption bands at 1.86 eV, 2.4 eV, and 2.9 eV as a superposition of the ligand field transitions Co(II) e→t_2 and Co(III) t_{2g}→e_g, which is, therefore, also the expected character for the two respective band gaps.

3 Supplementary material for TD-DFT calculations

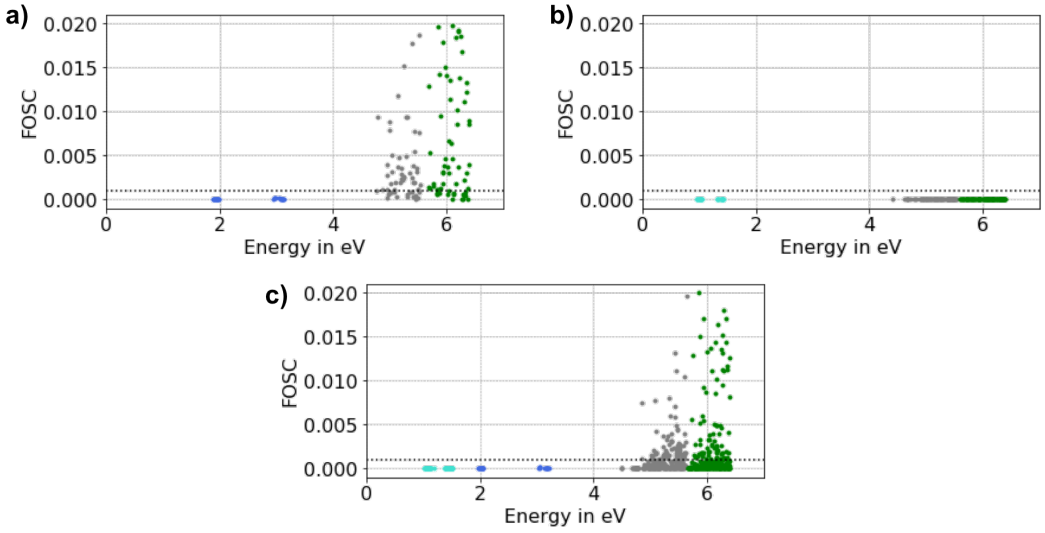

Figure S4. Excited states of Co_2ZnO_4 for system size 2t4o computed with TD-DFT with **a)** only singlet, **b)** only triplet, and **c)** spin-orbit coupled states. Level of theory: PBE0/def2-QZVPP. Color code: Co(III) 3d→3d triplet excitation (turquoise), Co(III) 3d→3d singlet excitation (blue), Co(III) 3d→Co(III) 3d MMCT (gray), O 2p→Co(III) 3d LMCT (green).

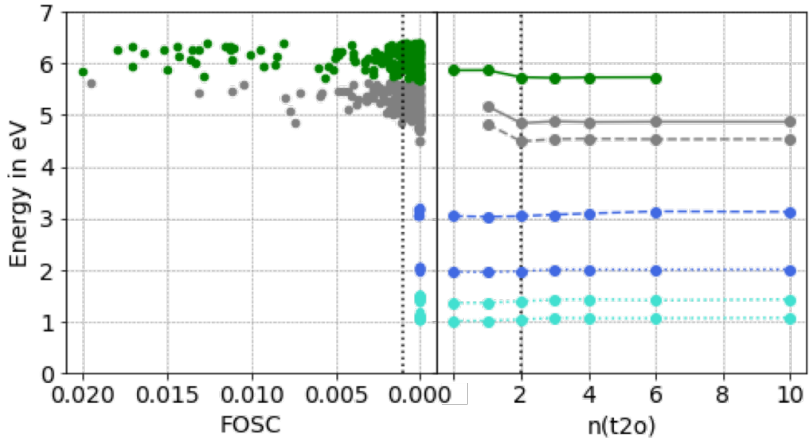

Figure S5. TD-DFT convergence scheme of Co_2ZnO_4 with PBE0/DKH-def2-tzvp. Color coding: Co(III) 3d t_{2g}→e_g triplet (turquoise) and singlet excitation (blue), Co(III) 3d→Co(III) 3d MMCT (gray), O 2p→Co(III) 3d LMCT (green); dark states (dotted line), "potentially" non-dark states (dashed line), non-dark states (solid line).

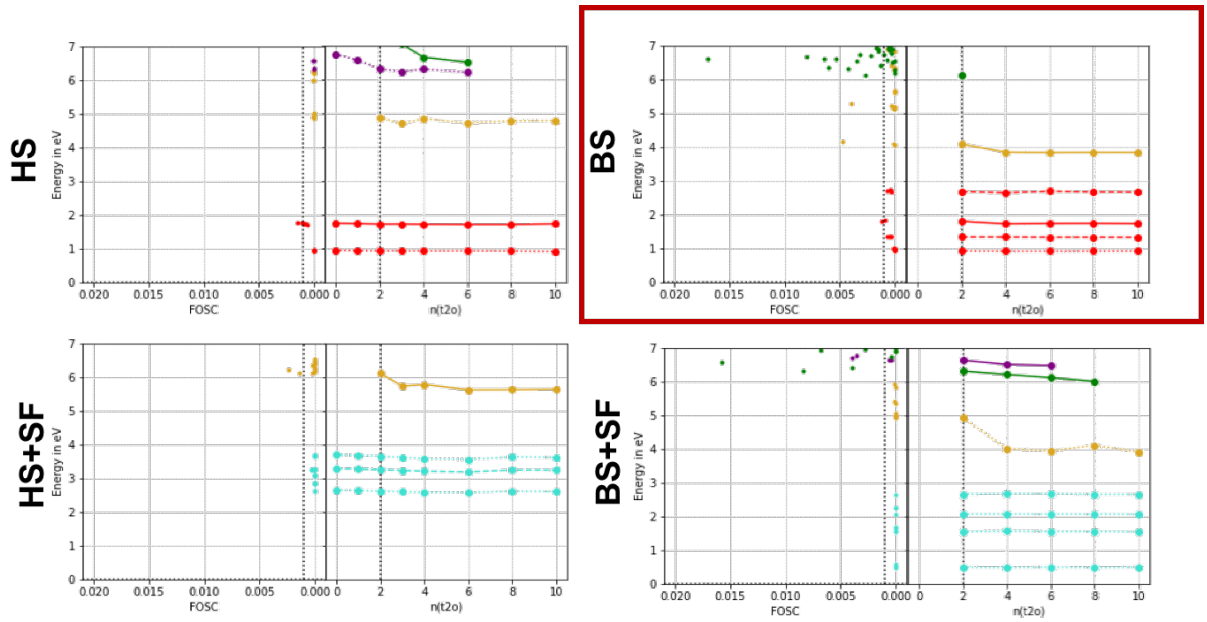

Figure S6. Different TD-DFT approaches to compute the states in Al_2CoO_4. Top left: high-spin (HS) approach, bottom left: HS with spin-flip (SF) approach, top right: broken-symmetry (BS), bottom right: BS with SF. Color coding: Co(II) d→d excitation (red), Co(II) d→d excitation with SF (turquoise), Co(II)→Co(II) MMCT (yellow), O 2p→Co(II) 3d LMCT (green), Co(II) 3d→4s (purple); dark states (dotted line), 'weakly' visible states (dashed line), visible states (solid line). BG_{opt1} about 1.4 eV (Co(II) d→d) and BG_{opt2} about 1.8 eV (Co(II) d→d). Level of theory: PBE0/def2-QZVPP.

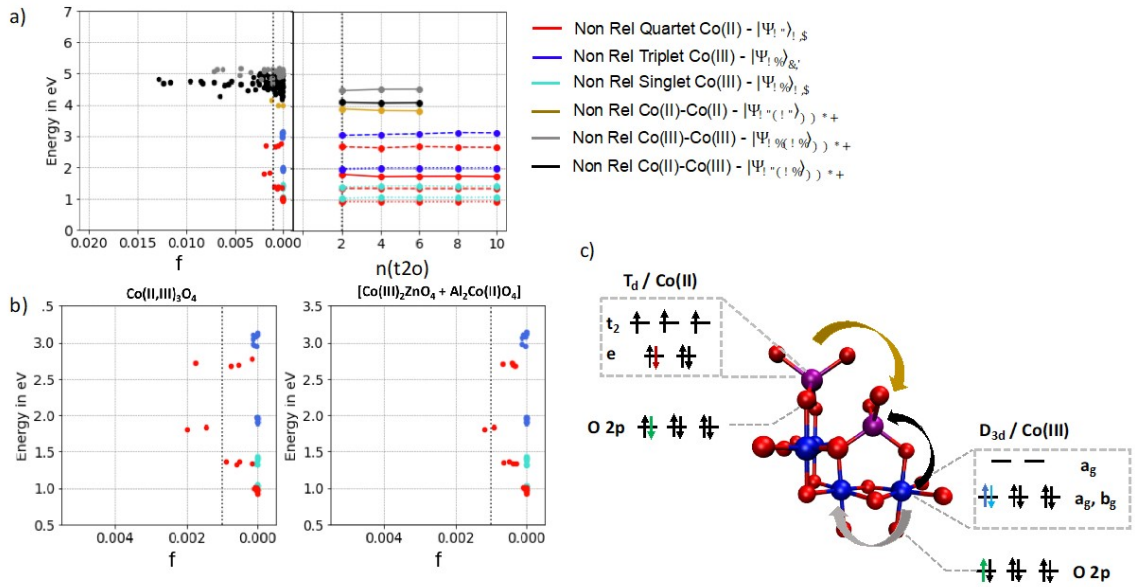

Figure S7. **a)** Broken-symmetry TD-DFT convergence scheme of Co_3O_4 with PBE0/DKH-def2-tzvp. **b)** Comparison Co ligand field excitations in Co_3O_4 (left) vs. [Co_2ZnO_4 + Al_2CoO_4] (right) computed with PBE0/DKH-def2-tzvp. Color coding: Co(II) 3d e→t_2 excitation (red), Co(III) 3d t_{2g}→e_g triplet (turquoise) and singlet excitation (blue), Co(III)→Co(III) M'M'CT (gray), Co(II)→Co(II) MMCT (yellow), Co(II)→Co(III) M'MCT/ M'MCT (black); dark states (dotted line), 'potentially' non-dark states (dashed line), non-dark states (solid line).

3.1 Comparison of single-reference methods (DFT, CIS, EOM-CC) and Literature

Based on the previous convergence model that showed that the energy range of the three band gaps in Co_3O_4, which are at 0.78 eV, 1.51 eV, and 2.14 eV experimentally, can be approached as the sum of the equivalent Al_2CoO_4 and Co_2ZnO_4 models, this section will reinvestigate the energy space of the two latter models with different DFT functionals as well as with CIS and EOM-CC to find a first explanation for the three band gaps. The approach is justified since a previous study[48] showed that the band gap converges for the DFT and EOM-CC models in identical ways.

As test calculations with reduced basis sets show, the current systems also converge equivalently for the different methods. Exceptions are the (meta-)GGA functionals. These functionals do not predict distinct bands between 0 eV and 3.5 eV. As the system size increases, the excited states build a continuum. Figure S7 demonstrates this exemplarily for the PBE functional for Co_3O_4, Al_2CoO_4, and Co_2ZnO_4. Although this indicates that this class of functionals cannot predict the excitation energies with the chosen approach, likely because of the missing XC functional crucial for TD-DFT excitation calculations, some features nevertheless converge with system size. Therefore, an interpretation of the converged potential band gaps is still possible, and the potential states will be considered in the following discussion of the results.

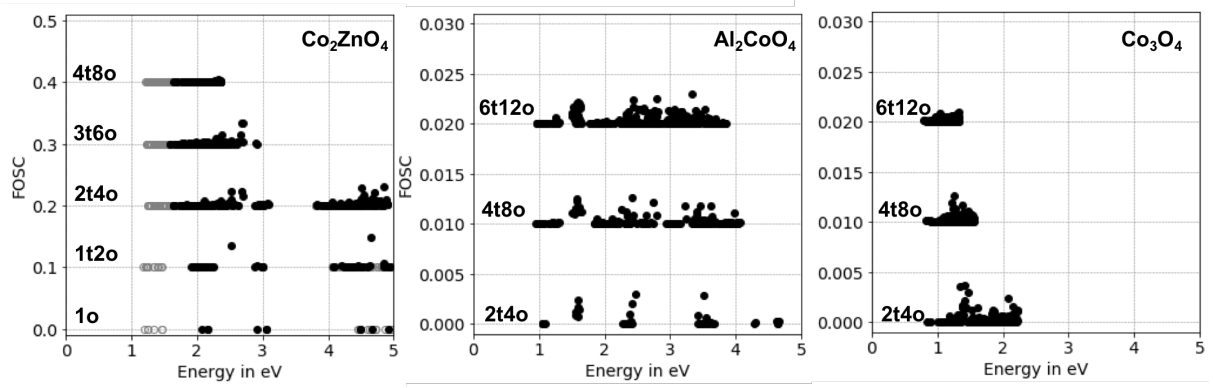

Figure S8. Excited states of increasing system size computed with PBE/def2-QZVPP for Co_2ZnO_4, Al_2CoO_4, and Co_3O_4.

The discussed PBE0 model, representative of all methods except (meta-)GGA, showed immediate convergence of the ligand field transitions in Co(II) and Co(III) at the smallest system sizes tested. However, the MMCT transitions in broken-symmetry Al_2CoO_4 models and all states in the (meta-)GGA models only converge for 4t8o. Therefore, for consistency, Figure S8 shows the first excited states of each absorption band representing the ligand field transitions and MMCT for QC size 4t8o. An exception is the EOM-CC result, calculated only for the isolated Co sites due to computational limitations and represents only the ligand field transitions. Since there is no option to calculate EOM-CC as broken-symmetry, the given EOM-CC Al_2CoO_4 result is high spin.

The empty circles in Figure S8 symbolize dark states with oscillator strengths between 0 and 0.0001, the half-filled circles represent states with oscillator strength between 0.0001 and 0.001, and the filled circles are non-dark states. The oscillator strength varies somewhat with the functionals. Nevertheless, all methods show a consistent picture regarding the type of excitations and their visibility.

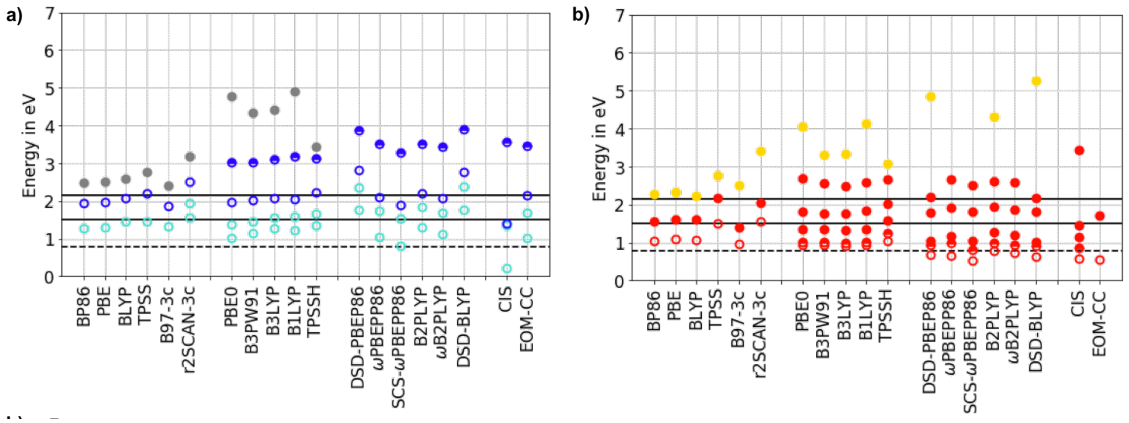

Figure S9. Results of excited states for TD-DFT for **a)** Co_2ZnO_4 and b) Al_2CoO_4 for QC size 4t8o (Exception: EOM-CC, QC sizes are 1o and 1t, respectively). Basis sets: def2-QZVPP. Color coding: Co(II) 3d e→t_2 (red), Co(III) Co(III) 3d t_{2g}→e_g triplet (turquoise) and singlet excitations (blue), Co(III)→Co(III) MMCT (gray), Co(II→Co(II) MMCT (yellow). Dark states (empty circle), "potentially" non-dark states (half-filled circles), non-dark states (filled circles).

In Figure S15, the band calculated with PBE0 at 0.9 eV, which is visible in the high spin case, and at 1.0 eV, which occurs in the broken symmetry model, were initially combined into one band for simplicity. However, they are shown as two bands in Figure S8b. While they overlap strongly for all hybrid functionals, they are distinguishable for double hybrid functionals and CIS. In addition, Figure S9 shows the results for CIS for the high spin case (2S+1=7) and the broken-symmetry cases (2S+1=5), (2+1=3), and (2+1=1), showing that all bands in the broken-symmetry model are original to the method and have slightly different energies than those in the high spin case. The intermediate spin states provide a combined picture that includes all states. However, since the affected bands still overlap significantly in all methods, Figure S8b shows only the lowest states in each case, as they are only relevant for the determination of the band gap.

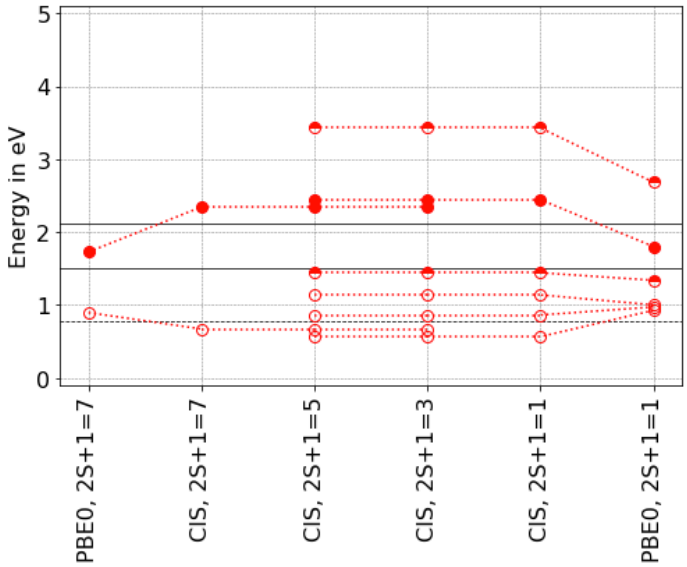

Figure S10. First excited states of ligand field transitions in Al_2CoO_4 with system size 2t4o computed as high spin (2S+1=7), intermediate spins (2S+1=5 and 2S+1=3), and open singlet (2S+1=1) with PBE0 and CIS.

In order to identify the source of the optical band gaps at 0.78 eV, 1.51 eV, and 2.14 eV, it is necessary to consider the calculated energy range from 0 eV to 3 eV. This range only includes the ligand field transitions in the tetrahedral Co(II) and distorted octahedral Co(III) centers for all hybrid functionals, double-hybrid functionals, CIS, and EOM-CC, indicating that they are likely to be the origin of the band gaps. The MMCT transitions typically occur at energies higher than 3 eV. Based on the oscillator strength, the ligand field transitions in Co(II) sites are (potentially) non-dark states and are dipole-allowed. In contrast, the Co(III) ligand field transitions in the same energy range are all dipole-forbidden dark states. However, the Co(III) ligand field transitions may contribute to or generate the band gaps by means of intensity borrowing mechanisms or by enhancing the Co(II) ligand field transitions, as indicated in Figure S15.

All (meta-)GGA functionals agree with the other methods that the band gaps at 0.78 eV and 1.51 eV originate from ligand field transitions. However, for the band gap at 2.14 eV, these functionals suggest the possibility that it may originate from a combination of Co(II)→Co(II) MMCT and dark singlet ligand field transitions of Co(III).

The experimental results do not exclude either perspective, the (meta-)GGA functionals or the other methods. Martens et al.[4] observed absorption bands at 0.8 eV, 1.6 eV, and 2.6 eV, which can be related to Co(II) or Co(III) or both. Kim et al.[46] observed that the features at 1.65 eV and 2.4 eV are essential for Co(II) sites, which could be due to the ligand field transition of Co(II) or the MMCT Co(II)→Co(II), among other possibilities.

Lima et al.[38] found that the band gaps at 1.51 eV and 2.14 eV computed with the hybrid functional B3PW91 originate from a superposition of ligand field transitions local to the Co(II) and Co(III) centers, which supports the current hybrid and double-hybrid functional results. In contrast, Xu

et al.[35] applied PBE and suggested Co(III)→Co(II) MMCT for the band gap at 2.14 eV, in agreement with the (meta-)GGA functionals used in this study.

All computational studies that analyzed the first excited state in the energy range of the band gap at 0.78 eV, such as Belova et al.[3], Miedzinska et al.[49], and Qiao et al.[26], agree that it can be characterized as a Co(II) ligand field transition. This agrees with all the methods used in the present study, as the first Co(II) ligand field transition always has a lower energy than the first Co(III) ligand field transition. Therefore, this transition can be considered the first excited state of Co_3O_4.

The transition types generally agree among the different methods, except for a few exceptions. However, their quantitative results are inconsistent and, therefore, inconclusive overall. None of the methods satisfactorily agrees with the experiments, and ambiguities remain concerning the assignment of states to specific band gaps.

4 Supplementary material for post-Hartree Fock calculations

Table S4. Dependence of the excited states on the basis set for different methods. Example system: 1t.

	State	def2-SVP	def2-TZVP	def2-QZVPP	cc-pVDZ	cc-pVTZ	cc-pVQZ	cc-pV5Z
PBE0	**3d→3d (1)**	0.899	0.945	0.976	0.897	0.957	0.979	0.987
	3d→3d (2)	1.736	1.744	1.763	1.718	1.749	1.766	1.773
	LMCT	6.386	6.740	6.653	6.085	6.629	6.681	6.695
EOM-CC	**3d→3d (1)**	0.444	0.494	0.529	0.485	0.504	0.525	0.530
	3d→3d (2)	1.699	1.751	1.733	1.759	1.731	1.748	1.755
	LMCT	7.471	7.422	7.478	7.255	7.395	7.610	7.700
SA-CASSCF	**3d→3d (1)**	0.415	0.441	0.442	0.413	0.434	0.443	-
	3d→3d (2)	0.717	0.763	0.764	0.712	0.748	0.766	-
	3d→3d (3)	2.746	2.749	2.749	2.730	2.743	2.748	-
NEVPT2	**3d→3d (1)**	0.481	0.545	0.547	0.500	0.539	0.550	-
	3d→3d (2)	0.818	0.923	0.929	0.843	0.910	0.936	-
	3d→3d (3)	2.406	2.351	2.262	2.356	2.281	2.235	-
MR-EOM-	**3d→3d (1)**	0.449	0.487	0.537	0.428	0.471	0.487	-
	3d→3d (2)	0.763	0.840	0.930	0.718	0.786	0.813	-
	3d→3d (3)	2.324	2.210	2.284	2.228	2.152	2.144	-

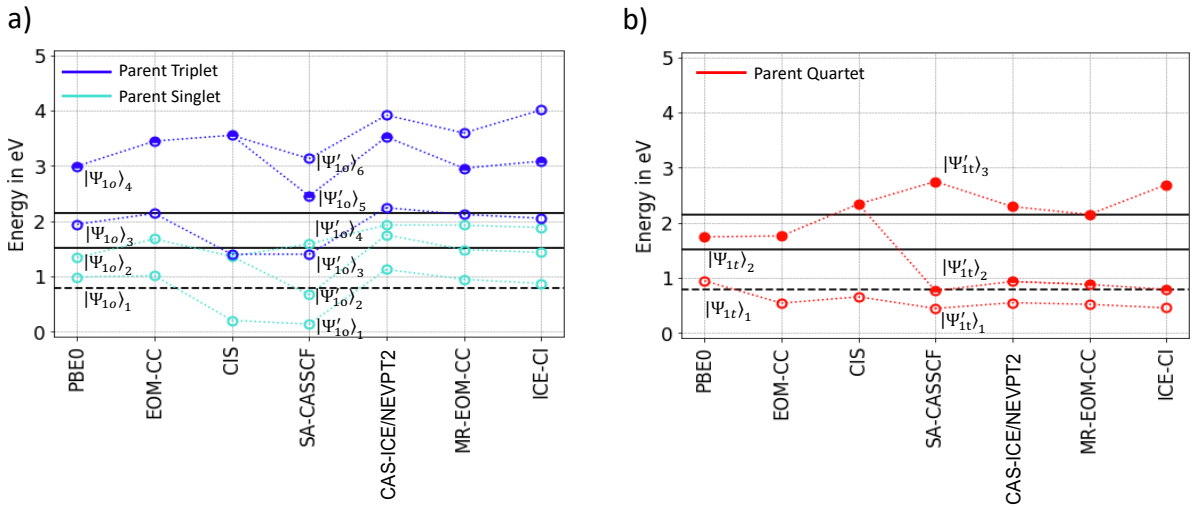

Figure S11. Description of the first excited triplet (turquoise) and singlet (blue) states of ligand field transitions in the isolated Co(III) site 1o in terms of single configurational methods (PBE0, EOM-CC, CIS) and with multiconfigurational methods (SA-CASSCF, NEVPT2, MR-EOM-CC, ICE-CI). Dark states (empty circle), "potentially" non-dark states (half-filled circles), non-dark states (filled circles).

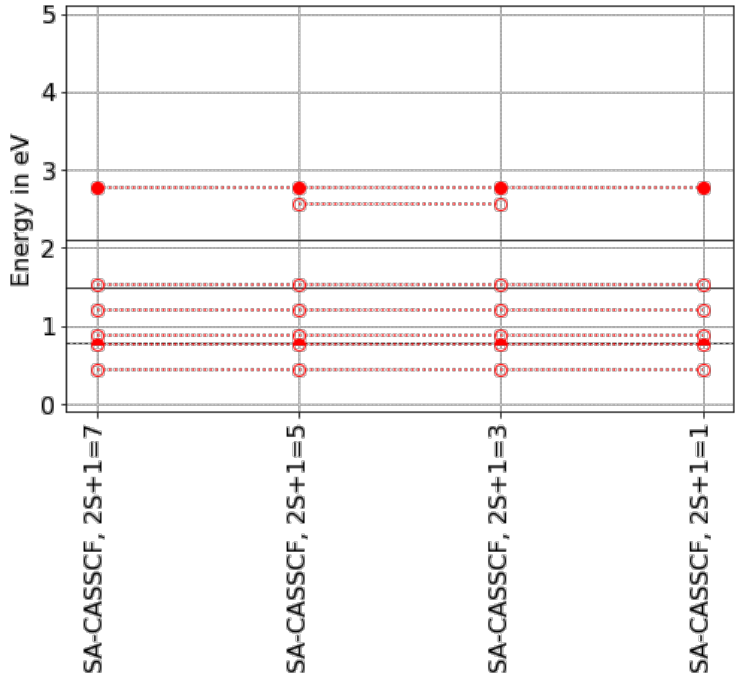

Figure S12. First excited states of ligand field transitions in Al_2CoO_4 with system size 2t4o computed as high spin (2S+1=7), intermediate spins (2S+1=5 and 2S+1=3), and open singlet (2S+1=1) with SA-CASSCF.

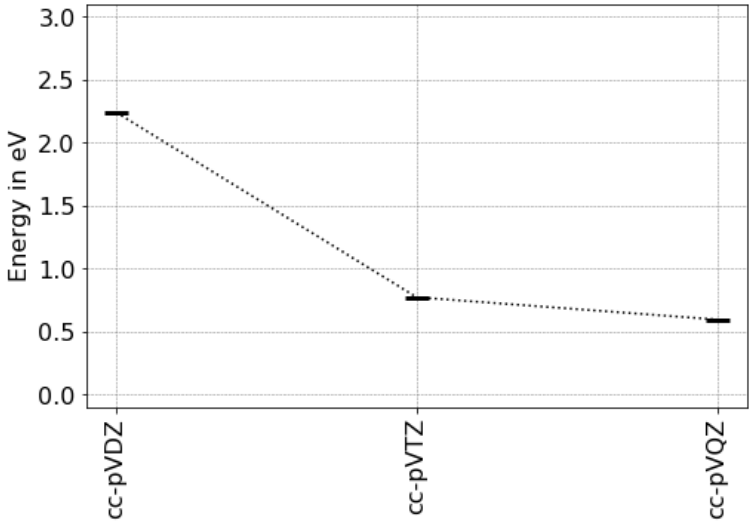

Figure S13. Energy difference between "neutral" and "ionic" antiferromagnetic ground states with increasing basis set size computed for system size 2t4o with NEVPT2.

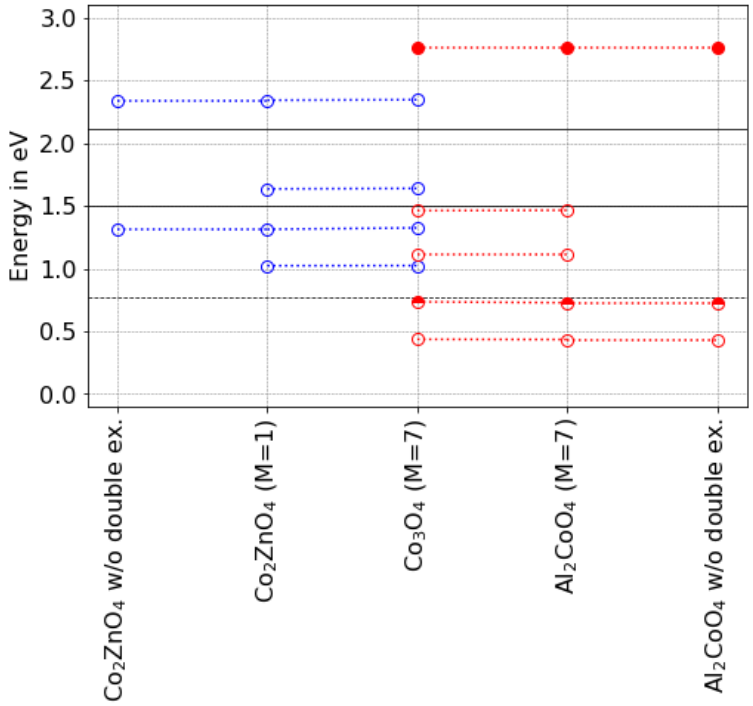

Figure S14. Excitations including double excitations in the different cobalt oxides calculated with ICE-CI/cc-pVTZ.

4.1 Comparison of different multireference methods

The MR-EOM-CC method has provided promising results in explaining the electronic properties of the different tetrahedral Co sites in the "ionic" and "neutral" antiferromagnetic model combined with the single octahedral Co(III) site. The calculated band gaps are in good agreement with experimental data, suggesting the validity of this approach. However, other multireference methods and their performance are worth considering, especially since the MR-EOM-CC method can only handle one tetrahedral Co site at a time. Other methods, such as SA-CASSCF/NEVPT2, as shown in the comparison above, or SA-CASSCF/CASPT2 can handle two Co sites simultaneously, making them potentially more representative of the actual antiferromagnetic states. Therefore, a comparison between MR-EOM-CC and other multireference methods could provide further insight into the electronic properties of these systems.

Figure S14 shows the multireference results for Co_2ZnO_4 and Al_2CoO_4, where Co_2ZnO_4 represents the octahedral and Al_2CoO_4 represents the tetrahedral Co sites in Co_3O_4. It should be noted that the results for Co_2ZnO_4 are obtained for only one Co(III) site, which has been demonstrated to be sufficient for all the methods thus far. However, for Al_2CoO_4, SA-CASSCF calculations are performed independently and with perturbation via NEVPT2, CASPT2, and DCD-CAS(2) for a two-center model. The "ionic" antiferromagnetic states are adjusted towards an optimal ideal superposition to the "neutral" state. The ICE-CI and MR-EOM-CC results are obtained for only one tetrahedral Co site at a time, with MR-EOM-CC being computationally limited. In contrast, ICE-CI is limited because it includes most valence oxygen orbitals. This is done to study the influence of orbitals other than the 3d orbitals, which

are only included in the active space in the other cases. The same applies to the ICE-CI result of Co_2ZnO_4.

To ensure clarity in the results presented in Figure S14, all excitations with double excitation characters in the octahedral Co(III) site have been excluded. Similarly, only the excitations relevant to the band gap are shown for the tetrahedral sites, along with the lowest dark state of the "neutral" antiferromagnetic case for reference.

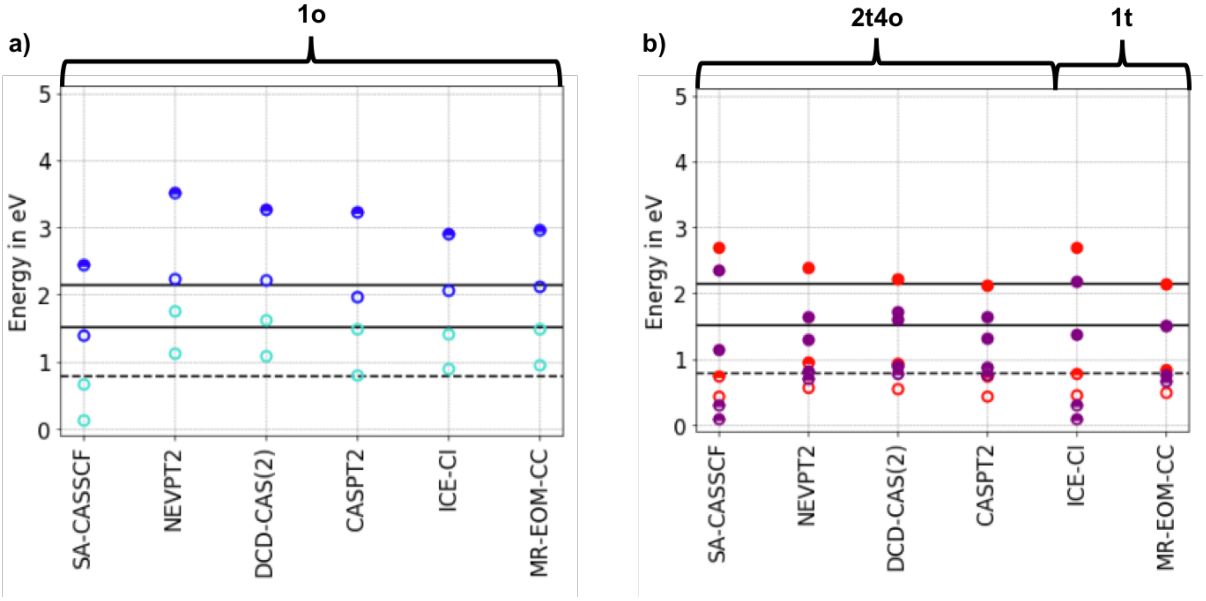

Figure S15. Results of ligand field excited states for mulifconfiguration/-reference methods for **a)** Co_2ZnO_4 and **b)** Al_2CoO_4. Color coding: tetrahedral Co 3d e→t_2 excitation for "neutral" (red) and for "ionic" (purple) antiferromagnetic states, octahedral Co 3d t_{2g}→e_g triplet (turquoise) and singlet (blue) excitations.

Qualitatively, the results describing the band gaps with tetrahedral sites are consistent for the "neutral" antiferromagnetic states. However, SA-CASSCF and ICE-CI do not accurately capture the behaviour of the "ionic" antiferromagnetic states, leading to an inaccurate representation of the band gaps in these models. For quantitative agreement with experimental results, methods that account for dynamic correlation are significantly more accurate than SA-CASSCF and ICE-CI. Among these methods, MR-EOM-CC provides the best agreement with experimental results in predicting the band gaps of systems with tetrahedral sites. This is due to its ability to accurately describe the excited states of the system by taking into account electron correlation, resulting in reliable predictions.

In the previous discussion of the MR-EOM-CC results, it was discovered that the first band gap observed experimentally at about 0.78 eV originates from the tetrahedral Co sites, particularly the one formally charged Co(III) in the "ionic" antiferromagnetic state. Although there are other excitations in this energy range, this specific excitation will be discussed for simplicity. MR-EOM-CC predicts a band gap of 0.76 eV. Excluding the ICE-CI and SA-CASSCF methods, which predict a band gap of about 0.31 eV, the multireference methods range from 0.71 eV for SA-CASSCF/NEVPT2 to 0.89 eV for SA-

CASSCF/DCD-CAS(2), with SA-CASSCF/CASPT2 providing the best result of 0.77 eV. It is important to note that two absorption bands are predicted in the vicinity of this band gap in the experiment. Therefore, the other competing excitations of differently charged tetrahedral Co centers may also contribute to the other absorption band.

MR-EOM-CC explained the experimental band gap at 1.51 eV by the presence of formally Co(I) and Co(III) tetrahedral sites in the "ionic" antiferromagnetic model, resulting in a calculated band gap of 1.51 eV from both sites. As already described and visualized in Figure 10, the two corresponding ligand field excitations have different energies when NEVPT2 is applied. This is also the case for all other methods tested. SA-CASSCF and ICE-CI again give ambiguous results due to the lack of dynamic correlation. According to the SA-CASSCF/NEVPT2 and SA-CASSCF/CASPT2 methods, the excited state of Co(III) is predicted to be at 1.31 eV and 1.32 eV, respectively, and the corresponding excited state of Co(I) is predicted to be at 1.65 eV. However, the DCD-CAS(2) method overestimates the band gap, placing the state originating from Co(III) state at 1.60 eV and the one from Co(I) at 1.73 eV.

The experimental band gap of 2.14 eV was in excellent agreement with the ligand field transition of high spin tetrahedral Co(II) calculated by MR-EOM-CC. The other multireference methods - again excluding SA-CASSCF and ICE-CI - vary from 2.12 eV for SA-CASSF/CASPT2 to 2.40 eV for SA-CASSCF/NEVPT2, with SA-CASSCF/DCD-CAS(2) placing the corresponding state at 2.22 eV.

As described above, the second triplet and first singlet ligand field excited states of the octahedral Co(III) sites represented by Co_2ZnO_4 calculated with EOM-CC show reasonable agreement with the band gaps at 1.51 eV and 2.14 eV, respectively. Switching to MR-EOM-CC improves the agreement, with calculated values of 1.49 eV and 2.12 eV. The results shown in Figure S14 support these findings, as SA-CASSCF/NEVPT2 (1.75 eV/2.24 eV) and SA-CASSCF/CASPT2 (1.62 eV/2.22 eV) slightly overestimate the two band gaps, while SA-CASSCF/CASPT2 (1.49 eV/1.97 eV) and ICE-CI (1.42 eV/2.06 eV) slightly underestimate them. This suggests that although the ligand field transition states of the octahedral site are formally considered dipole-forbidden "dark states" and, thus, have zero or near-zero oscillator strength, they may still contribute to the two band gaps in conjunction with the ligand field transitions of the tetrahedral sites. This could happen either by gaining intensity themselves or by enhancing the intensity of the tetrahedral ligand field excitations.

The idea of a superposition of the octahedral and tetrahedral ligand field excitations has already been entertained in the TD-DFT discussion and is also based on Lima et al.[38] The contribution of the octahedral ligand field excitations may also explain the experimental evidence for Co(III) sites, such as in the higher absorption peak associated with the second band gap. Kim et al.[46] showed that this feature in Co_3O_4 shifted from 2.40 eV to 2.80 eV for Co_2ZnO_4. In all tested computational methods, the second band of singlet states in Co_2ZnO_4 gains more oscillator strength. These states appear at 2.96 eV in the MR-EOM CC calculations and may explain this observation.

Notably, the first bands of the triplet states of the octahedral ligand field excitations are close to the first band gap of 0.78 eV. Although overestimation occurs in all methods, including dynamic correlation, except SA-CASSCF/CASPT2, which agrees well with the band gap, this finding suggests that the octahedral sites may also play a role in this case or, more likely, contribute to the higher absorption band found experimentally in this energy range (peak at about 0.94 eV).

While the multireference description may provide an overall more satisfactory description of the cobalt oxides that is in better agreement with the experiments than TD-DFT, the drawback is that certain states, such as the MMCT states, are not included in the final model due to computational limitations. In addition, the approach is restricted to smaller cluster sizes. Thus, the combination of the two approaches provides not only competing but also concordant explanations, leading to a more rounded overall explanation. In general, the two protocols provide a valuable complementary approach.

5 Derivation of the Hubbard Correlation Hamiltonian in BO Framework

We start from the 2-electron Hamiltonian in the Born-Oppenheimer approximation

$$H_{BO} = \sum_{p,q} h_{pq}\hat{E}_{pq} + 1/2 \sum_{p,q,r,s}(pq|rs)\,\hat{E}_{pq}\hat{E}_{rs} - \delta_{qr}\hat{E}_{ps})$$

in which, p,q,r,s are general orbital indices, $\hat{E}_{pq}$ is the excitation operator defined as

$$\hat{E}_{pq} = \sum_{\sigma\in\{\alpha,\beta\}} \hat{\alpha}^{\dagger}_{p\sigma}\hat{\alpha}_{q\sigma}$$

with spin $\sigma \in \{\alpha, \beta\}$, and creation $\hat{\alpha}^{\dagger}_{p\sigma}$ and $\hat{\alpha}_{q\sigma}$ the creation and annihilation operators which create and annihilate an electron in orbitals p and q with spin σ respectively. h_{pq} are the 1-electron orbital energies and $(pq|rs)$ are 2-electron integrals. Hence using anticommutation relations and normal order of operators H_{BO} is given by:

$$H_{BO} = \sum_{p,q} h_{pq \sum_{\sigma}\hat{\alpha}^{\dagger}_{p\sigma}\hat{\alpha}_{q\sigma}} + 1/2 \sum_{p,q,r,s}\sum_{\sigma,\sigma'}(pq|rs)\,\hat{\alpha}^{\dagger}_{p\sigma}\hat{\alpha}^{\dagger}_{r\sigma'}\hat{\alpha}_{q\sigma}\hat{\alpha}_{s\sigma'}$$

Considering that Coulomb J_{pq} and Exchange K_{pq} 2-electron integrals are given by

$$J_{pq} = (pp|qq) = \iint \left|\varphi_p\,(\mathrm{r}_1)\right|^2 \frac{1}{\mathrm{r}_{12}} \left|\varphi_q\,(\mathrm{r}_2)\right|^2, \mathrm{d}r_1\mathrm{d}r_2$$

$$K_{pq} = (pq|qp) = \iint \varphi^*_p(\mathrm{r}_1)\varphi^*_q(\mathrm{r}_2)\frac{1}{\mathrm{r}_{12}}\varphi_{\mathrm{q}}\,(\mathrm{r}_1)\psi_{\mathrm{p}}\,(\mathrm{r}_2)\,, \mathrm{d}r_1\mathrm{d}r_2$$

Hence by retaining only, the dominant contributions arising by on-site A-A or B-B and inter-site A-B interactions we can derive the needed terms for the Hubbard Hamiltonian. Hence for the 1-electron terms one has:

1) On-site terms. The 1-electron term for (p = q) reads:

$$\sum_{p} h_{pp\,\sum_{\sigma}\hat{\alpha}^{\dagger}_{p\sigma}\hat{\alpha}_{p\sigma}} = n_p h_{pp} \equiv h^{eff}_{pq}$$

where h_{pp} represent the crystal field energies, (e.g. E_e^{CoII}, E_{t2}^{CoII}, E_{eg}^{CoIII}, E_{t2g}^{CoIII} or E^{O} when an O Ligand is considered) and $n_p$is the electron occupancy. While the 2-electron Coulomb repulsion term, (p = q, r = s):

$$\sum_{p}(pp|pp)\sum_{\sigma,\sigma\prime}\ \hat{\alpha}^{\dagger}_{p\sigma}\hat{\alpha}^{\dagger}_{p\sigma\prime}\hat{\alpha}_{p\sigma}\hat{\alpha}_{p\sigma\prime} = \sum_{p} J_{pp}\left(\sum_{\sigma}\ \hat{\alpha}^{\dagger}_{p\sigma}\hat{\alpha}^{\dagger}_{p\sigma}\right)\left(\sum_{\sigma\neq\sigma\prime}\ \hat{\alpha}^{\dagger}_{p\sigma\prime}\hat{\alpha}^{\dagger}_{p\sigma\prime}\right) \equiv J^{eff}_{pp}$$

2) Nearest-Neighbour terms. This involves the hopping 1-electron term

$$\sum_{p,q}\left\{h_{pq\,\sum_{\sigma}\left(\hat{\alpha}^{\dagger}_{p\sigma}\right\}\hat{\alpha}_{p\sigma}+\hat{\alpha}^{\dagger}_{q\sigma}\hat{\alpha}_{p\sigma}}\right) \equiv -t_{pq}$$

where $h_{pq} = -t_{pq}$ represent the hopping integral (e,g, $t_{AA,}$ $t_{AB,}$ or $t_{AO,}$ t_{AO}, when an O Ligand is considered)

As well as the respective two electron Coulomb repulsion and Exchange terms:

Coulomb repulsion term, (p = q, r = s, p ≠ r):

$$\sum_{p\neq q}(pp|qq)\sum_{\sigma,\sigma\prime}\ \hat{\alpha}^{\dagger}_{p\sigma}\hat{\alpha}^{\dagger}_{p\sigma\prime}\hat{\alpha}_{q\sigma}\hat{\alpha}_{q\sigma\prime} = \sum_{p\neq q} J_{pq}\left(\sum_{\sigma}\ \hat{\alpha}^{\dagger}_{p\sigma}\hat{\alpha}^{\dagger}_{p\sigma}\right)\left(\sum_{\sigma\neq\sigma\prime}\ \hat{\alpha}^{\dagger}_{q\sigma\prime}\hat{\alpha}^{\dagger}_{p\sigma\prime}\right) \equiv J^{eff}_{pq}$$

Exchange term, (p = r, q = s):

$$-\sum_{p,q}(pq|qp)\sum_{\sigma,\sigma\prime}\ \hat{\alpha}^{\dagger}_{p\sigma}\hat{\alpha}^{\dagger}_{q\sigma\prime}\hat{\alpha}_{p\sigma\prime}\hat{\alpha}_{q\sigma} = -\sum_{p,q} K_{pq\,\sum_{\sigma}\left\{(\hat{\alpha})^{\dagger}_{p\sigma}\hat{\alpha}^{\dagger}_{q\bar{\sigma}}\hat{\alpha}_{p\bar{\sigma}}\hat{\alpha}_{q\sigma}+h.c.\right)\equiv -K^{eff}_{pq}}$$

where $\overline{\sigma}$ = β if σ = α

Hence the Hubbard Hamiltonian in the BO framework reads

$$H^{BO}_{Hubbard} = \underbrace{h^{eff}_{pp} + J^{eff}_{pp}}_{On-Site}\underbrace{-t_{pq} + J^{eff}_{pq} - K^{eff}_{pq}}_{Inter-Site}$$

It follows that by setting $h_{pp} = 0$, and $J_{pp} = \mathrm{U}$, and omitting the Inter-Site Coulmb and Exchange terms one arrives to the original Hubbard Hamiltonian model.

$$H_{Hubbard}^{Original} = \underbrace{U^{eff}}_{On-Site} + \underbrace{-t_{pq}}_{Inter-Site}$$

There are in principle 5 predominant site interaction terms namely: 1) the on-site crystal field energies h_{pp} (e.g. $\varepsilon_e^{Co(II)}$, $\varepsilon_{t2}^{Co(II)}$, $\varepsilon_{eg}^{Co(III)}$, $\varepsilon_{t2g}^{Co(III)}$ or ε_p^O when an O Ligand is considered. 2) the on-site Coulomb repulsion J_{pp} 3) the inter-site hopping integral t_{pq} (e.g. $t_{AA,}$ $t_{AB,}$ or $t_{AO,}$ when an O Ligand is considered), 4) the inter-site Coulomb repulsion J_{pq} and 5) the inter-site exchange term K_{pq}.

5.1 Numerical Model Example

Let us now employ the above interaction Hamiltonian in a simple numerical example. We define a model system starting from the 'neutral' antiferromagnetic ground state configuration state function CSF $|\Psi_N\rangle \equiv |\mathrm{A_p}: \mathrm{e}^4\mathrm{t}_2^3, \mathrm{B}: \mathrm{t}_{2\mathrm{g}}^6, \mathrm{A_q}: \mathrm{e}^4\bar{\mathrm{t}}_2^3\rangle$, we consider in addition the d-d excited state $|\Psi_{\mathrm{ES}}\rangle$: $|\mathrm{A_p}: \mathrm{e}^3\mathrm{t}_2^4, \mathrm{B}: \mathrm{t}_{2\mathrm{g}}^6, \mathrm{A_q}: \mathrm{e}^4\bar{\mathrm{t}}_2^3\rangle$, the LMCT ionic state $|\Psi_{\mathrm{LMCT}}\rangle$: $|\mathrm{O}: \mathrm{p}^5, \mathrm{A_p}: \mathrm{e}^4\mathrm{t}_2^4, \mathrm{B}: \mathrm{t}_{2\mathrm{g}}^6, \mathrm{A_q}: \mathrm{e}^4\bar{\mathrm{t}}_2^3\rangle$, the A-A MMCT ionic state $|\Psi_{\mathrm{MMCT}}^{\mathrm{A-A}}\rangle$: $|\mathrm{A_p}: \mathrm{e}^4\mathrm{t}_2^2, \mathrm{B}: \mathrm{t}_{2\mathrm{g}}^6, \mathrm{A_q}: \mathrm{e}^4\bar{\mathrm{t}}_2^4\rangle$, the A-B MM'CT ionic state $|\Psi_{\mathrm{MM'CT}}^{\mathrm{A-B}}\rangle$: $|\mathrm{A_p}: \mathrm{e}^4\mathrm{t}_2^2, \mathrm{B}: \mathrm{t}_{2\mathrm{g}}^6\mathrm{e}_{\mathrm{g}}^1, \mathrm{A_q}: \mathrm{e}^4\bar{\mathrm{t}}_2^3\rangle$, and the B-A M'MCT ionic state $|\Psi_{\mathrm{M'MCT}}^{\mathrm{B-A}}\rangle$: $|\mathrm{A_p}: \mathrm{e}^4\mathrm{t}_2^3, \mathrm{B}: \mathrm{t}_{2\mathrm{g}}^5, \mathrm{A_q}: \mathrm{e}^4\mathrm{t}_2^1\bar{\mathrm{t}}_2^3\rangle$, where bar indicate spin-down electron occupancies and p and q are general orbital indices. These states can mix on the basis of the Hubbard Hamiltonian.

We recall that a two-state system with a neutral and ionic state that are allowed to mix. Their Energy difference is $\Delta E = E_N - E_I$ and the mixing Hamiltonian matrix is: $\mathrm{H} = \begin{pmatrix} E_N & V \\ V & E_I \end{pmatrix}$, where $\mathrm{V} = \langle\Psi_{\mathrm{N}}|H|\Psi_{\mathrm{I}}$. It follows that the resulted mixed states are: $|\Psi_{\pm}\rangle = c_N^{\pm}|\Psi_N\rangle + c_I^{\pm}|\Psi_I$,

with energies $E_{\pm} = \frac{E_N+E_I}{2} \pm \sqrt{\left(\frac{\Delta E}{2}\right)^2 + V^2}$, with $c_{N,I}$ the respective mixing coefficients:

$c_N^{\pm} = \frac{1}{\sqrt{1+\left(\frac{E_N-E_{\pm}}{V}\right)^2}}$, $c_I^{\pm} = \frac{E_N-E_{\pm}}{V} c_N^{\pm}$. In this concept we can distinguish the following interaction cases:

5.1.1 d-d transitions at A (or B) sites

Considering first A sites, regular ligand field (LF) d-d transitions on A sites will give rise on a set of excited states state $|\Psi_{ES}\rangle$: $|A_p: \mathrm{e}^3\mathrm{t}_2^4, \mathrm{B}: \mathrm{t}_{2\mathrm{g}}^6, A_q: \mathrm{e}^4\bar{\mathrm{t}}_2^3\rangle$. This is an intra-site process, not involving direct electron transfer between sites A_p and A_q. Hence the energies of the d-d excited states in this model are given by $\Delta E_{ES-N}^{\pm} = \frac{\Delta\varepsilon_{tetrahedral}}{2} \pm \sqrt{\left(\frac{\Delta\varepsilon_{tetrahedral}}{2}\right)^2 + \left(t_{pAqA} + K_{pAqA}\right)^2}$.

Both $t_{pAqA} < 10^{-2}$ and $K_{pAqA} < 10^{-5}$ are very small, owning to the fact that 1) the ground state antiferromagnetic coupling is very small, and 2) the two sites are not nearest neighbours, they are separated by Co(III) B-sites, rendering the inter-site d-overlap, and consequently t_{ApAq} very small. This also indicate minimum mixing between the ground and excited states. As a result the excitation energy is given by $\Delta E_{ES-N} \sim \Delta\varepsilon_{tetrahedral} \sim 0.81$ eV which for the Co(II) A centres amount to about 1eV. This is consistent with the lowest energy BG. As expected, the impact of the electron correlation is negligible, hence is not surprising that this energy gap is well reproduced already at the CASSCF level calculations. In a similar fashion it can be shown that at B-sites $\Delta E_{ES-N} \sim \Delta\varepsilon_{octahedral}$, which fall out of the energy range of the observed BGs while they result in negligible intensities.

5.1.2 LMCT transitions at A sites

In the case of LMCT transitions we consider:

- the neutral ground state $|\Psi_N\rangle$: $|O: p^6, A_p: \mathrm{e}^4\mathrm{t}_2^3, \mathrm{B}: \mathrm{t}_{2\mathrm{g}}^6, A_q: \mathrm{e}^4\bar{\mathrm{t}}_2^3\rangle$
- the d-d excited state $|\Psi_{ES}\rangle$: $|O: p^6, A_p: \mathrm{e}^3\mathrm{t}_2^4, \mathrm{B}: \mathrm{t}_{2\mathrm{g}}^6, A_q: \mathrm{e}^4\bar{\mathrm{t}}_2^3\rangle$
- the LMCT ionic state $|\Psi_{LMCT}\rangle$: $|O: p^5, A_p: \mathrm{e}^4\mathrm{t}_2^4, \mathrm{B}: \mathrm{t}_{2\mathrm{g}}^6, A_q: \mathrm{e}^4\bar{\mathrm{t}}_2^3\rangle$

In the first approximation we consider only the interaction between the ground state $|\Psi_N$ and the LMCT one $|\Psi_{LMCT}$. Hence the interaction Hamiltonian reads:

$$\mathrm{H} = \begin{pmatrix} 0 & V_{LMCT} \\ V_{LMCT} & E_{LMCT} \end{pmatrix} = \begin{pmatrix} 0 & t_{pAlO} + K_{pAlO} \\ t_{pAlO} + K_{pAlO} & J_{pOpO} + J_{pAlO} + (\varepsilon_{3dA} - \varepsilon_{2pO}) \end{pmatrix}$$

Where:

- $V_{LMCT} = t_{pAlO} + K_{pAlO}$
- $E_{LMCT} = J_{pOpO} + J_{pAlO} + (\varepsilon_{dA} - \varepsilon_{pO})$

Hence the energy gap referring to the LMCT transitions is $\Delta E_{LMCT} = 2\sqrt{\left(\frac{E_{LMCT}}{2}\right)^2 + V_{LMCT}^2}$

Considering in addition the d-d excited state the interaction Hamiltonian reads

$$H = \begin{pmatrix} 0 & 0 & V_{N-LMCT} \\ 0 & \Delta\varepsilon_{tetrahedral} & V_{LMCT} \\ V_{N-LMCT} & V_{LMCT} & E_{LMCT} \end{pmatrix}$$

$$= \begin{pmatrix} 0 & 0 & t_{pAlO} \\ 0 & \Delta\varepsilon_{tetrahedral} & t_{pAlO} + K_{pAlO} \\ t_{pAlO} & t_{pAlO} + K_{pAlO} & J_{pOpO} + J_{pAlO} + (\varepsilon_{3dA} - \varepsilon_{2pO}) \end{pmatrix}$$

We can now make use

1) of the bare CASSCF 1- and 2-electron integrals

2) the factor of ~4 fold NEVPT2 versus CASSCF energy stabilization of the LMCT states (as described at section VII of the main text) and perform a numerical substitution of the above interaction Hamiltonian.

Solving the resulting eigenvalue problem gives numerical estimates for E_{ES} and E_{LMCT}, summarized in Table S5. The numerical example shows that the ES and LMCT states mix by about 10% and 20% before and after applying the NEVPT2 energy stabilization to the bare CASSCF 2-electron integrals with the stabilization reflected to the E_{ES} energies from the $\Delta\varepsilon_{tetrahedral}$ value. In both cases the

E_{LMCT} falls into the 2.5-4.5 eV range, consistent with the CASSCF and NEVPT results presented in section VII.

Table S5. Numerical evaluation employing a Hubbard like model Hamiltonian to a set of chosen ES and LMCT CSFs to represent the predominant d-d, and LMCT transitions.

Terms (eV)	Using bare CASSCF 1- and 2-electron integrals	Prescreening the Coulomb integrals from the NEVPT2 energy stabilization
$\Delta\varepsilon_{tetrahedral}$	0.81	0.81
$\varepsilon_{dA} - \varepsilon_{pO}$	1.81	1.81
t_{pAlO}	-1.25	-1.25
J_{pOpO}	4.80	1.20
J_{pAlO}	3.53	0.88
K_{pAlO}	0.14	0.14
E_{ES}	0.77	0.71
E_{LMCT}	4.44	2.69

5.1.3 MMCT transitions at A and B sites

In the case of MMCT transitions we consider

- the neutral ground state $|\Psi_N\rangle$: $|: \mathrm{e}^4\mathrm{t}_2^3, \mathrm{B}: \mathrm{t}_{2\mathrm{g}}^6, A_q: \mathrm{e}^4\bar{\mathrm{t}}_2^3\rangle$
- the d-d excited state $|\Psi_{ES}\rangle$: $|A_p: \mathrm{e}^3\mathrm{t}_2^4, \mathrm{B}: \mathrm{t}_{2\mathrm{g}}^6, A_q: \mathrm{e}^4\bar{\mathrm{t}}_2^3\rangle$
- the A-A' MMCT ionic state $|\Psi_{MMCT}^{A-A'}\rangle$: $|A_p: \mathrm{e}^4\mathrm{t}_2^2, \mathrm{B}: \mathrm{t}_{2\mathrm{g}}^6, A_q: \mathrm{e}^4\bar{\mathrm{t}}_2^4\rangle$
- the A-B MM'CT ionic state $|\Psi_{MM'CT}^{A-B}\rangle$: $|A_p: \mathrm{e}^4\mathrm{t}_2^2, \mathrm{B}: \mathrm{t}_{2\mathrm{g}}^6\mathrm{e}_{\mathrm{g}}^1, A_q: \mathrm{e}^4\bar{\mathrm{t}}_2^3\rangle$
- the B-A M'MCT ionic state $|\Psi_{M'MCT}^{B-A'}\rangle$: $|A_p: \mathrm{e}^4\mathrm{t}_2^3, \mathrm{B}: \mathrm{t}_{2\mathrm{g}}^5, A_q: \mathrm{e}^4\mathrm{t}_2^1\bar{\mathrm{t}}_2^3\rangle$

Hence by taking into account the interaction between the ground state $|\Psi_N\rangle$ and the A-A' MMCT $|\Psi_{MMCT}^{A-A}\rangle$ A-B MMCT $|\Psi_{MM'CT}^{A-B}\rangle$ and B-A M'MCT $|\Psi_{M'MCT}^{B-A}\rangle$ as well as he interaction with the d-d excited state $|\Psi_{ES}\rangle$: $|A_p: \mathrm{e}^3\mathrm{t}_2^4, \mathrm{B}: \mathrm{t}_{2\mathrm{g}}^6, A_q: \mathrm{e}^4\bar{\mathrm{t}}_2^3\rangle$ The interaction Hamiltonian reads:

$$H = \begin{pmatrix} 0 & 0 & V_{A-A'} & V_{A-B} & V_{B-A'} \\ 0 & \Delta\varepsilon_{tetrahedral} & V_{ES-A-A'} & V_{ES-A-B} & V_{ES-B-A'} \\ V_{A-A'} & V_{ES-A-A} & E_{MMCT}^{A-A'} & V_{A-A'-A-B} & V_{A-A'-B-A'} \\ V_{A-B} & V_{ES-A-B} & V_{A-B-A-A'} & E_{MM'CT}^{A-B} & V_{A-B-B-A'} \\ V_{B-A'} & V_{ES-B-A'} & V_{B-A'-A-A'} & V_{B-A'-A-B} & E_{M'MCT}^{B-A'} \end{pmatrix}$$

Where

- $E_{MMCT}^{A-A'} = \Delta\varepsilon_{AA} + (\underbrace{7J_{pA'qA'} - 6J_{pAqA}}_{On-Site\ Coulomb}) + \underbrace{(J_{pAqA'} + 6J_{pBqA'} - 6J_{pAqB'})}_{Inter-Site\ Coulom}$
- $E_{MM'CT}^{A-B} = \Delta\varepsilon_{AB} + (\underbrace{-6J_{pA'qA'} + 6J_{pBqB}}_{On-Site\ Coulomb}) + \underbrace{(-7J_{pAqA'} + 7J_{pBqA'})}_{Inter-Site\ Coulom}$
- $E_{M'MCT}^{B-A} = \Delta\varepsilon_{AB} + (\underbrace{-5J_{pBqB} + 7J_{pA'qA'}}_{On-Site\ Coulomb}) + \underbrace{(-7J_{pAqB} + 7J_{pAqA'} - 2J_{pBqA'})}_{Inter-Site\ Coulom}$
- $V_{A-A'} = t_{pAqA'}, V_{A-B} = t_{pAqB}, V_{B-A'} = t_{pBqA'}$
- $V_{ES-A-A} = t_{pAqA'} + K_{pAqA'}, V_{ES-A-B} = t_{pAqB} + K_{pAqB}, V_{ES-B-A'} = t_{pBqA'} + K_{pBqA'}$
- $V_{A-A'-A-B} = t_{pAqB}, V_{A-A'-B-A'} = t_{pBqA'}, V_{A-B-B-A'} = K_{pAqB} + K_{pBqA'}$

Like in the LMCT case described in section 5.1.2 we can now

1) Utilize the bare CASSCF 1- and 2-electron integrals.

2) Incorporate the ~9-fold factor of NEVPT2 versus CASSCF energy stabilization of the MMCT states (see Section VII of the main text) and perform a numerical substitution of the resulting interaction Hamiltonian. Solving the corresponding eigenvalue problem yields a numerical estimation of the transition energies: E_{ES}, E_{MMCT}^{A-A} *and* $E_{MM'CT}^{A-B}/E_{M'MCT}^{B-A}$.

The results are summarized in Table S6.

Table S6. Numerical evaluation employing a Hubbard like model Hamiltonian to a set of chosen ES and LMCT CSFs to represent the predominant d-d, and LMCT transitions.

Terms (eV)	Using bare CASSCF 1- and 2-electron integrals	Prescreening the 2-elctron integrals from the NEVPT2 energy stabilization
$\Delta\varepsilon_{tetrahedral}$	0.81	0.81
$\Delta\varepsilon_{AA'}$	0.01	0.01
$\Delta\varepsilon_{AB}$	1.36	1.36
$\Delta\varepsilon_{BA}$	1.36	1.36
J_{pAqA}	23.7	2.63
$J_{pA'qA'}$	23.7	2.63
J_{pBqB}	15.3	1.70
$t_{pAqA'}$	1.25	1.25
t_{pAqB}	$<5\text{x}10^{-3}$	$<5\text{x}10^{-3}$
$t_{pBqA'}$	$<5\text{x}10^{-3}$	$<5\text{x}10^{-3}$
$J_{pAqA'}$	3.80	0.42
J_{pAqB}	4.08	0.45
$J_{pBqA'}$	4.08	0.45
$K_{pAqA'}$	0.90	0.90
K_{pAqB}	$<10^{-4}$	$<10^{-4}$
$K_{pBqA'}$	$<10^{-4}$	$<10^{-4}$
E_{ES}	0.77	0.81
$E_{MMCT}^{A-A'}$	23.71	2.64
$E_{MM'CT}^{A-B}$	16.66	3.06
$E_{M'MCT}^{B-A'}$	22.35	1.28

The numerical example above demonstrates that when the Coulomb integrals are scaled by a factor of ~9 according to the NEVPT2 versus CASSCF energy stabilization, all MMCT energies fall within the 1.5-2.5 eV range, aligning with the middle energy experimental BG. Similar to the LMCT numerical example, a ~20% mixing with the LF transitions at site A is crucial for achieving good agreement with the experimental data.

6 Supplementary material for ground state magnetic structure of Co_3O_4

Before proceeding to the excited state calculations, the magnetic structure of Co_3O_4 in the ground state is discussed. It has been shown experimentally that in the ground state of Co_3O_4 the Co(II) sites are weakly antiferromagnetically coupled with J = -2 to -5 cm^{-1}.

6.1 Principles of two center ground state magnetic coupling

The magnetic properties of a system comprised of two interacting magnetic centers with fictitious local spins $\mathbf{S}_A$ and $\mathbf{S}_B$ are typically interpreted in the context of the phenomenological Heisenberg–Dirac–van Vleck spin-Hamiltonian:

$$\hat{\mathrm{H}}_{\mathrm{HDvV}} = -2J_{AB}\hat{S}_A\hat{S}_B \tag{1}$$

where the J_{AB} is the coupling constant or the exchange integral between nuclei centers A and B, while $\hat{S}_A$ and $\hat{S}_B$ are the corresponding spin operators. In practice, the effective exchange coupling constant J in Eq. 1 serves as a measure of the strength of the interaction and is positive for a ferromagnetic and negative for an antiferromagnetic spin alignment.

As shown previously[50-53] in the description of antiferromagnetic coupling, apart from the 'neutral' states in which the groups of antiparallel coupled electrons are localized in the involved magnetic centers, one has to consider all relevant 'ionic' states in which only a fraction of the antiparallel coupled electrons are localized in the involved magnetic centers. In the conventional description, these 'ionic' states can be reached from the 'neutral' states by metal to metal or metal to ligand charge transfer (MMCT or MLCT). The net result is a more complete description of the electron correlation phenomena in these systems, which further stabilizes the dominant 'neutral' antiferromagnetic states.

The well-studied problem[51, 53] of two centers A and B, each carrying an unpaired electron and occupying the two singly occupied canonical orbitals and . (e.g., the case of the Cu(II) dimer) can demonstrate the 'ionic' and 'neutral' antiferromagnetic states. The two centers can couple to one triplet and three singlet states, which can be represented by a set of four configuration state functions (CSFs), e.g. constructed by the genealogical coupling scheme, to form two 'neutral' $\left|\,^3\Phi\right\rangle = |+\,+\rangle$, $\left|\,^1\Phi\right\rangle = |\pm\rangle$ and two 'ionic' $\left|\,^1\Phi\right\rangle = |2\;0\rangle$, $\left|\,^1\Phi\right\rangle = |0\;2\rangle$ CSFs. By localizing the t and u singly occupied orbitals, one can form the corresponding magnetic orbitals $\mathrm{a} = \frac{1}{\sqrt{2}}(\mathrm{t}+\mathrm{u})$ and $\mathrm{b} = \frac{1}{\sqrt{2}}(\mathrm{t}-\mathrm{u})$, which are local to the respective centers A and B. In this context, the singlet-triplet energy difference can be evaluated as the expectation value of the BO Hamiltonian for these CSFs, which before CI amounts to

$$\mathrm{E}(S=0) - \mathrm{E}(\mathrm{S}=1) = 2K_{ab} \equiv J_{AB} \tag{2}$$

where $K_{ab} = \int \psi_a(r_1)\psi_b(r_2)\frac{1}{r_{12}}\psi_a(r_2)\psi_b(r_1)dr_1dr_2$ is the inter-site exchange integral between the magnetic orbitals a and b of the respective centers. Configuration interaction can further mix the 'neutral' and 'ionic' states so that expression (2) becomes:

$$\mathrm{E}(S=0) - \mathrm{E}(S=1) = 2K_{ab} - \frac{4F_{ab}^2}{J_{aa}-J_{ab}} \equiv J_{AB} \tag{3}$$

where $J_{aa} = \int \psi_a(r_1)\psi_b(r_2)\frac{1}{r_{12}}\psi_a(r_2)\psi_b(r_1)dr_1dr_2$ is the intra-site exchange integral, $J_{ab} = \int \psi_a(r_1)\psi_b(r_2)\frac{1}{r_{12}}\psi_a(r_2)\psi_b(r_1)dr_1dr_2$ is the inter-site coulomb integral, and F_{ab} is the inter-site Fock like integral (section 5.5). It becomes evident that for systems consisting of centers with a higher number of spins, the effective exchange coupling constant *J* is associated with the pairwise spin interactions across the components of the entire spin ladder. [54, 55] For the case of Co_3O_4 this will be elaborated in the following section.

6.2 Origin of magnetic coupling in Co3O4

In a first approximation, the analysis is restricted to a model cluster of the Co_3O_4 crystal structure consisting of two Co(II) and one Co(III) center. Starting with only the two Co(II) centers in mind, the problem can be set up as two $S = \frac{3}{2}$ systems interacting to give a spin ladder $S = 0,1,2,3$. One can construct the CSFs representing the neutral configurations for each of the spin states. Following the genealogical coupling scheme, for a given spin multiplicity more than one CSF can be constructed, giving one, five, nine, and five CSFs for the septet, quintet, triplet, and singlet states, respectively, as shown:

$$|{}^7_I\Phi_N\rangle, |{}^5_I\Phi_N\rangle, |{}^3_I\Phi_N\rangle, |{}^1_I\Phi_N\rangle$$

Evaluating the expectation value of the BO Hamiltonian for the neutral CSFs (see Section 5.5), the energy differences between the spin states are:

$$\mathrm{E}(S=3) - \mathrm{E}(S=2) = -\frac{1}{2}\overline{K}_{tu}{}^{5}A_{tu} \quad (4)$$

$$\mathrm{E}(S=2) - \mathrm{E}(S=1) = \frac{1}{2}\overline{K}_{tu}\left({}^{5}A_{tu} - {}^{3}A_{tu}\right) \quad (5)$$

$$\mathrm{E}(S=1) - \mathrm{E}(S=0) = \frac{1}{2}\overline{K}_{tu}\left({}^{3}A_{tu} - {}^{1}A_{tu}\right) \quad (6)$$

where ${}_I{}^{2S+1}A_{pq} = \langle {}^{2S+1}_I\Phi_N | E^p_q E^q_p | {}^{2S+1}_J\Phi_N$ and $\overline{K}_{tu} = \frac{1}{2}\sum_t^{SOMOs}\sum_{u\neq t}^{SOMOs} K_{tu}$.

As shown in Table S5 comparison with the energy separation obtained by modelling this system with the HDvV Hamiltonian provides the magnitude of J~J_0 as a function of exchange integrals $\overline{K}_{tu}$ and coupling coefficients ${}^{2S+1}A_{pq}$.

Table S5. Comparison of the energy differences between the components of the spin ladder in Co_3O_4 on the basis of the model HDvV Hamiltonian and the expectation values of the BO Hamiltonian.

	ΔE(S-(S-1)) (H_{HDvV})	ΔE(S-(S-1)) (H_{BO})
S=3	-6 J	$-\frac{1}{2}\bar{K}_{tu}\,{}^{5}A_{tu}$
S=2	-4 J	$\frac{1}{2}\bar{K}_{tu}\left({}^{5}A_{tu}-{}^{3}A_{tu}\right)$
S=1	-2 J	$\frac{1}{2}\bar{K}_{tu}\left({}^{3}A_{tu}-{}^{1}A_{tu}\right)$
S=0	0	0

This simple model can be further improved by considering the mixing between the neutral CSFs of same spin multiplicity, but different spin couplings. Inclusion of this mixing gives an additional contribution to J, J_1:

$$J_1 = \frac{\frac{1}{2}\bar{K}_{tu}\,{}^{2S+1}_{IJ}A_{tu}}{\Delta E\left({}^{2S+1}_{I}\Phi_N - {}^{2S+1}_{J}\Phi_N\right)} \qquad (7)$$

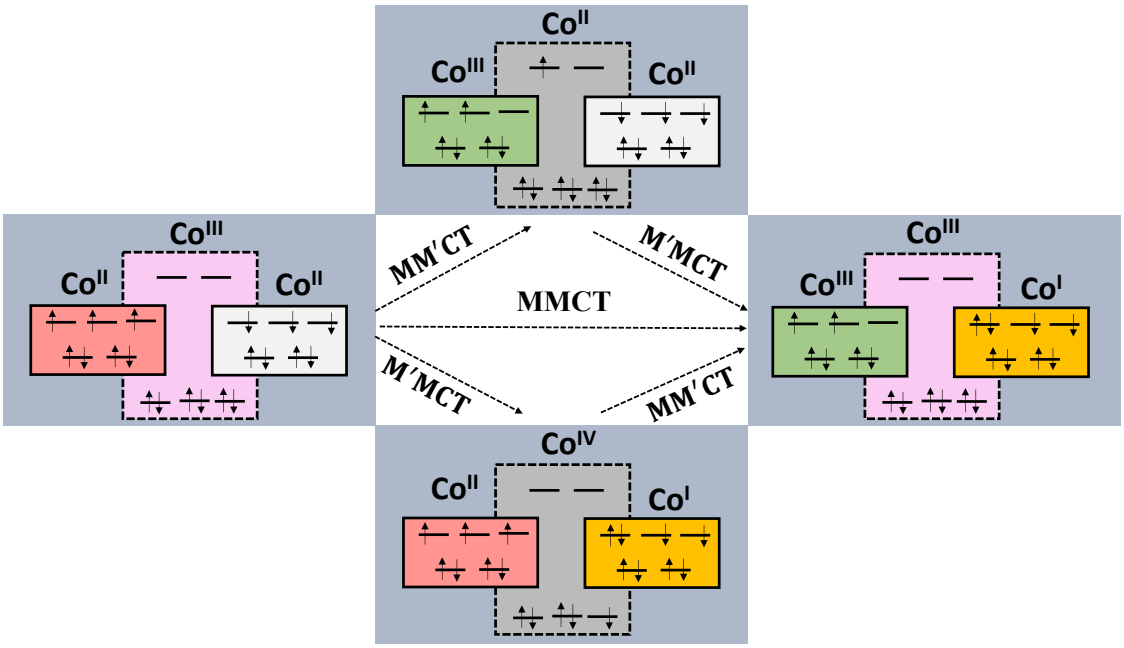

Figure S16. Schematic representation of the possible coupling MMCT pathways between 'neutral' and 'ionic' states.

Focusing on Co_3O4 and in particular on the simplified model 2t1o, which contains two tetrahedrally coordinated $M = Co^{II}$ centers antiferromagnetically coupled and bridged by an octahedrally coordinated LS $M' = Co^{III}$ center, there are in principle three MMCT-type transitions from the 'neutral' antiferromagnetic ground state to 'ionic' states, as shown in Figure S15. 1) via direct MMCT transitions $Co^{II} \cdots Co^{III} \cdots Co^{II} \rightarrow Co^{III} \cdots Co^{III} \cdots Co^{I}$ between the formal Co^{II} centers and 2) via indirect MM′CT/M′MCT sequencies of transitions between the Co^{II} centers and Co^{III} centers resepctively:

$$\mathrm{MM'CT/M'MCT: Co^{II} \cdots Co^{III} \cdots Co^{II} \rightarrow Co^{III} \cdots Co^{II} \cdots Co^{II} \rightarrow Co^{III} \cdots Co^{III} \cdots Co^{I}}$$

$$\mathrm{M'MCT/MM'CT: Co^{II} \cdots Co^{III} \cdots Co^{II} \rightarrow Co^{II} \cdots Co^{IV} \cdots Co^{I} \rightarrow Co^{III} \cdots Co^{III} \cdots Co^{I}}$$

Inclusion of these CSFs result in the following additional contributions to J:

$$J_2 = \frac{t_{tu}}{\Delta E\left({}^{2S+1}\Phi_{ion} - {}^{2S+1}\Phi_N\right)} \quad (8)$$

$$J_3 = \frac{t_{ta}}{\Delta E\left({}^{2S+1}\Phi_{MM'CT} - {}^{2S+1}\Phi_N\right)} \quad (9)$$

$$J_4 = \frac{t_{it}}{\Delta E\left({}^{2S+1}\Phi_{M'MCT} - {}^{2S+1}\Phi_N\right)} \quad (10)$$

where $t_{pq} = \left\langle \Phi_I \middle| \widehat{H} \middle| \Phi_J \right\rangle$ is the hopping integral, while *i, a* and *t, u* represent doubly occupied, virtual and singly occupied orbitals respectively. Collectively the $\mathrm{J} \equiv J_{total}$ can be provided by the following expression:

$$\mathrm{J} \equiv J_{total} = J_0 + J_1 + J_2 + J_3 + J_4 \quad (11)$$

6.3 Numerical evaluation of *J* on the basis of Broken Symmetry DFT

As a first approximation, one can resort to the broken symmetry (BS)DFT approach.[53, 56-66] In this concept, in contrast to the above description, the antiferromagnetic state is reflected in a single unrestricted determinant, where the singly occupied opposite-spin 'magnetic orbitals' are allowed to take spatial parts that are more or less localized at the magnetic centers. The (BS)DFT calculated charge density is usually within acceptable limits, although the spin density obtained from the determinant is qualitatively incorrect.[53, 56, 57]

In principle, there are several spin projection approaches to map the DFT-BS energies onto those of the Heisenberg Hamiltonian states[53], which are categorized according to their ability to reproduce the *J* coupling constant in the wide range between weak and strong interactions[61, 65, 67-69]. Among them, the Yamaguchi formula[67, 68] is somewhat preferred, since it is valid for both regimes of weak and strong coupling interactions. Since the preference of the equations under discussion is still debated in the literature, the performance of different approaches is evaluated below for their ability to calculate the weak antiferromagnetic coupling between the two Co(II) centers in Co_3O_4.

In the case of Co_3O_4 the results are summarized in Table S6. All tested functionals ranging between non-hybrid (BP86, PBE, BLYP), hybrid (B3LYP, PBE0) and double-hybrid (wPBEPP86, SCS-wPBEPP86 and DSD-BLYP) predict the correct sign of J in three commonly employed approximations (Noodleman[61], Gatteschi[65, 69] and Yamaguchi[67, 68]). However, unless hybrid functionals are employed all other functionals outperform.

Table S6. BS-DFT computed J values in a variety of functionals and approximations.

J /Functional	BP86	PBE	BLYP	PBE0	B3LYP	wPBEPP86	SCS-wPBEPP86	DSD-BLYP

$J_{Noodleman}$	-9.52 cm^{-1}	-9.94 cm^{-1}	-11.12 cm^{-1}	-4.90 cm^{-1}	-5.18 cm^{-1}	-1.53 cm^{-1}	-1.53 cm^{-1}	-1.54 cm^{-1}
$J_{Gatteschi}$	-7.14 cm^{-1}	-7.46 cm^{-1}	-8.34 cm^{-1}	-3.76 cm^{-1}	-3.88 cm^{-1}	-1.15 cm^{-1}	-1.15 cm^{-1}	-1.15 cm^{-1}
$J_{Yamaguchi}$	- 9.51 cm^{-1}	-9.94 cm^{-1}	-11.11 cm^{-1}	-4.89 cm^{-1}	-5.18 cm^{-1}	-1.53 cm^{-1}	-1.53 cm^{-1}	-1.54 cm^{-1}

6.4 Numerical evaluation of *J* on the basis of Approximate CI

Further insight into the exact mechanism of the antiferromagnetic coupling in Co_3O_4 is sought in the CAS-ICE and CAS-ICE/NEVPT2 level theories, which can naturally treat all necessary 'neutral' and 'ionic' antiferromagnetic states required for the evaluation of the coupling constant by Eq. 4 -11.

In this concept evaluating the Dirac–van Vleck spin-Hamiltonian (1) requires the determination of the energies of the entire spin-ladder (S = 0, 1, 2, 3) components.[54, 55] The results are summarized in Table S7. The first step is to focus on an active space that includes only the two Co(II) centers (CAS(14,10)). This provides access to all ‘neutral’ and ‘ionic’ MMCT states within the Co(II) centers in the 2t1o cluster. While the order of the spin ladder energies is correctly predicted, leading to the correct sign of *J*, their magnitude is strongly underestimated, leading to unphysically small *J* values compared to experiment. The situation changes rapidly when the active space is extended to include all relevant MMCT and MLCT transitions involving the Co(III) centers CAS(20,15). As shown in Table S7, especially at the CAS-ICE/NEVPT2 level the calculated *J* value (*J* = -4.98) is in very good agreement with the experiment.

Table S7. CAS-ICE and CAS-ICE /NEVPT2 computed spin-ladder energies and J values employing Dirac–van Vleck spin-Hamiltonian (1).

Spin Ladder/J	Model	CAS-ICE	CAS-ICE /NEVPT2
	CAS(14,10)		
S = 0	0	0	0
S = 1	-2 J	0.9 cm^{-1}	2.4 cm^{-1}
S = 2	-6 J	2.7 cm^{-1}	3.9 cm^{-1}
S = 3	-12 J	5.5 cm^{-1}	8.7 cm^{-1}
J	-5.05 cm^{-1}	-0.66 cm^{-1}	-1.07 cm^{-1}
	CAS(20,15)		
S = 0	0	0	0
S = 1	-2 J	6.8 cm^{-1}	10.2 cm^{-1}
S = 2	-6 J	20.2 cm^{-1}	30.1 cm^{-1}
S = 3	-12 J	41.1 cm^{-1}	61.2 cm^{-1}
J	-5.05 cm^{-1}	-3.35 cm^{-1}	-4.98 cm^{-1}

In conclusion, it has been shown that an excellent description of the antiferromagnetic ground state of Co_3O_4 can be achieved once all relevant 'neutral' and 'ionic' antiferromagnetic states are properly taken into account. The extent to which this might influence the excited state energies that probe the optical band gap in Co_3O_4 is discussed in the main text.

7 Input file examples

7.1 Broken-Symmetry TD-DFT input file

```
!VeryTightSCF Ionic-Crystal-QMMM PBE0 RIJCOSX DKH2 DKH-def2-qzvpp def2/J def2-qzvpp/C

%scf maxiter 500
Flipspin 4,5
FinalMs 0.0
end

%tddft
  maxiter 500
  nroots 200
  PrintLevel 3
end

%qmmm
 QMAtoms {0:26} end
 ORCAFFFilename "2t4o.ORCAFF.prms"
  HFLayers 0
  ECPLayerECP "SDD"
  ECPLayers 3
  CONV_Charges false
  ENFORCETOTALCHARGE true
  CHARGE_TOTAL    0
  PrintLevel 4
end


*xyzfile -26 7 2t4o.xyz
```

7.2 EOM-CC with HFLayer input file

```
!Ionic-Crystal-QMMM UHF EOM-CCSD RIJCOSX DKH2 cc-pVQZ-DK def2/J cc-pVQZ/C RI-SOMF(1x)

%scf maxiter 500 end

%mdci
  iroot 1
  maxiter 500
  nroots 20
end


%qmmm
 QMAtoms {0} end
 ORCAFFFilename "1t.ORCAFF.prms"
  HFLayerAtoms {1:4} end
  ECPLayerECP "SDD"
  ECPLayers 3
  CONV_Charges false
  ENFORCETOTALCHARGE true
  CHARGE_TOTAL    0
  PrintLevel 4
end

*xyzfile 2 4 1t.xyz
```

7.3 SA-CASSCF with NEVPT2 input file

```
!Ionic-Crystal-QMMM cc-pVQZ/C def2/J DKH2 cc-pVQZ-DK
!NoITER NormalPrint MOREAD NoLoewdin NoMulliken


%moinp "2t4o.gbw"


%casscf
nel 14
norb 10
nroots 200
mult 1
maxiter 100
PTMethod SC_NEVPT2
end

%qmmm
 QMAtoms {0:26} end
 ORCAFFFilename "2t4o.ORCAFF.prms"
  HFLayers 0
  ECPLayerECP "SDD"
  ECPLayers 4
  CONV_Charges false
  ENFORCETOTALCHARGE true
  CHARGE_TOTAL    0
  PrintLevel 4
end


*xyzfile -26 7 2t4o.xyz
```

7.4 MR-EOM-CC input file

```
!MR-EOM Ionic-Crystal-QMMM cc-pVQZ/C def2/J DKH2 cc-pVQZ-DK
!NoITER NormalPrint MOREAD NoLoewdin NoMulliken

%moinp "1t.gbw"

%casscf
nel 7
norb 5
nroots 20
mult 4
maxiter 100
ActOrbs unchanged
end

%mrci
newblock 4*
nroots 20
 refs cas(7,5) end
end
soc
 dosoc true
end
end

%qmmm
 QMAtoms {0:4} end
 ORCAFFFilename "1t.ORCAFF.prms"
  HFLayers 0
  ECPLayerECP "SDD"
  ECPLayers 3
  CONV_Charges false
  ENFORCETOTALCHARGE true
  CHARGE_TOTAL    0
  PrintLevel 4
end


*xyzfile -6 4 1t.xyz
```

8 References

1. A. E. Cherkashin and F. I. Vilesov, *Sov. Phys. Solid State*, 1969, **11**, 1068.
2. T. Tanaka, *Jpn. J. Appl. Phys.*, 1979, **18**, 1043-1047.
3. I. D. Belova, Y. E. Roginskaya, R. R. Shifrina, S. G. Oagarin, Y. V. Plekhanov and Y. N. Venevtsev, *Solid State Commun*, 1983, **47**, 577-584.
4. J. W. D. Martens, W. L. Peeters and H. M. van Noort, *J. Phys. Chem. Solids*, 1985, **46**, 411-416.
5. J. G. Cook and M. P. van der Meer, *Thin Solid Films*, 1986, **144**, 165-176.
6. W. A. Murad, S. M. Al-Shamari, F. H. Al-Khateeb and R. H. Misho, *Phys. Stat. Sol. (a)*, 1988, **106**, 143-146.
7. L. Schumacher, I. B. Holzhueter, I. R. Hill and M. J. Dignam, *Electrochim. Acta*, 1990, **35**, 975-984.
8. A. J. Varkey and A. F. Fort, *Sol. Energy Mater. Sol. Cells*, 1993, **31**, 277-282.
9. M. Lenglet and C. K. Jørgensen, *Chem. Phys. Lett.*, 1994, **229**, 616-620.
10. P. Nkeng, G. Poillerat, J. F. Koenig, P. Chartier, B. Lefez, J. Lopitaux and M. Lenglet, *J. Electrochem. Soc.*, 1995, **142**, 1777-1783.
11. P. S. Patil, L. D. Kadam and C. D. Lokhande, *Thin Solid Films*, 1996, **272**, 29-32.
12. P. Ruzakowski Athey, F. K. Urban III, M. F. Tabet and W. A. McGahan, *J. Vac. Sci. Technol. A*, 1996, **14**, 685-692.
13. C.-S. Cheng, M. Serizawa, H. Sakata and T. Hirayma, *Mater. Chem. Phys.*, 1998, **53**, 225-230.
14. D. Barreca, C. Massignan, S. Daolio, M. Fabrizio, C. Piccirillo, L. Armelao and E. Tondello, *Chem. Mater.*, 2001, **13**, 588-593.
15. L. D. Kadam and P. S. Patil, *Mater. Chem. Phys.*, 2001, **68**, 225-232.
16. B. Pejova, A. Isahi, M. Najdoski and I. Grozdanov, *Mater. Res. Bull.*, 2001, **36**, 161-170.
17. K. J. Kim and Y. R. Park, *Solid State Commun.*, 2003, **127**, 25-28.
18. A. U. Mane and S. A. Shivashankar, *J. Cryst. Growth*, 2003, **254**, 368-377.
19. A. Gulino, G. Fiorito and I. Fragalà, *J. Mater. Chem.*, 2003, **13**, 861-865.
20. H. Yamamoto, S. Tanaka and K. Hirao, *J. Appl. Phys.*, 2003, **93**, 4158-4162.
21. N. Bahlawane, E. Fischer Rivera, K. Kohse-Höinghaus, A. Brechling and U. Kleineberg, *Appl. Catal. B*, 2004, **53**, 245-255.
22. V. R. Shinde, S. B. Mahadik, T. P. Gujar and C. D. Lokhande, *Appl. Surf. Sci.*, 2006, **252**, 7487-7492.
23. S. Thota, A. Kumar and J. Kumar, *Mater. Sci. Eng. B*, 2009, **164**, 30-37.
24. P. H. T. Ngamou and N. Bahlawane, *Chem. Mater.*, 2010, **22**, 4158-4165.
25. A. Louradi, A. Rmili, F. Ouachtrai, A. Couaoud, B. Elidrissi and H. Erguig, *J. Alloys Compd.*, 2011, **509**, 9183-9189.
26. L. Qiao, H. Y. Xiao, H. M. Meyer, J. N. Sun, C. M. Rouleau, A. A. Puretzky, D. B. Geohegan, I. N. Ivanov, M. Yoon, W. J. Weber and M. D. Biegalski, *J. Mater. Chem. C*, 2013, **1**, 4628-3633.
27. M. M. Waegle, H. Q. Doan and T. Cuk, *J. Phys. Chem. C*, 2014, **118**, 3426-2432.
28. C.-M. Jiang, L. R. Baker, J. M. Lucas, J. Vura-Weis and A. P. Alivisatos, *J. Phys. Chem. C*, 2014, **118**, 22774-22784.
29. K. P. Reddy, R. Jain, M. K. Ghosalya and C. S. Gopinath, *Journal Of Physical Chemistry C*, 2017, **121**, 21472-21481.
30. A. Lakehal, B. Bedhiaf, A. Bouaza, H. Benhebal, A. Ammari and C. Dalache, *Mater. Res.*, 2018, **21**, e20170545.
31. Y. Zhang, J. Ge, B. Mahmoudi, S. Förster, F. Syrowatka, A. W. Maijenburg and R. Scheer, *ACS Appl. Energy Mater.*, 2020, **3**, 3755-3769.

32. K. M. E. Miedzinska, B. R. Hollebone and J. G. Cook, *J. Phys. Chem. Solids*, 1987, **48**, 649-656.
33. L. Wang, T. Maxisch and G. Ceder, *Phys. Rev. B*, 2006, **73**.
34. A. Walsh, S.-H. Wei, Y. Yan, M. M. Al-Jassim, J. A. Turner, M. Woodhouse and B. A. Parkinson, *Phys. Rev. B*, 2007, **76**, 165119.
35. X.-L. Xu, Z.-H. Chen, Y. Li, W.-K. Chen and J.-Q. Li, *Surf. Sci.*, 2009, **603**, 653-658.
36. J. Chen, X. Wu and A. Selloni, *Phys. Rev. B*, 2011, **83**, 245204.
37. A. Montoya and B. S. Haynes, *Chem. Phys. Lett.*, 2011, 63-68.
38. A. F. Lima, *J. Phys. Chem. Solids*, 2014, **75**, 148-152.
39. V. Singh, M. Kosa, K. Majhi and D. T. Major, *Journal Of Chemical Theory And Computation*, 2015, **11**, 64-72.
40. G. A. Kaptagay, T. M. Inerbaeva, Y. A. Mastrikovb, E. A. Kotominb and A. T. Akilbekova, *Solid State Ion.*, 2015, **277**, 77-82.
41. A. F. Lima, *J. Phys. Chem. Solids*, 2016, **91**, 86-89.
42. N. H. M. Zaki, M. Mustaffa, M. F. M. Taib, O. H. Hassan, M. Z. A. Yahya and A. M. M. Ali, *Int. J. Eng. Technol.*, 2018, **7**, 121-125.
43. O. M. Sousa, J. S. Lima, A. F. Lima and M. V. Lalic, *J. Magn. Magn. Mater* 2019, **484**, 21-30.
44. V. S. Zhandun and A. Nemtsev, *J. Magn. Magn. Mater.*, 2020, **499**, 166306.
45. A. Cadi-Essadeka, A. Roldana, D. Santos-Carballala, P. E. Ngoepeb, M. Claeysc and N. H. de Leeuw, *S. Afr. J. Chem.*, 2021, **74**.
46. K. J. Kim and Y. R. Park, *Solid State Commun.*, 2003, **127**, 25–28.
47. J. P. Perdew, *Phys. Rev. B*, 1986, **33**, 8822-8824.
48. A. Dittmer, R. Izsák, F. Neese and D. Maganas, *Inorg. Chem.* , 2019, **58**, 9303-9315.
49. K. M. E. Miedzinska, B. R. Hollebone and J. G. Cook, *J. Phys. Chem. Solids*, 1987, **48**, 649—656.
50. P. De Loth, P. Cassoux, J. P. Daudey and J. P. Malrieu, *Journal of the American Chemical Society*, 1981, **103**, 4007-4016.
51. F. Neese, *Journal of Physics and Chemistry of Solids*, 2004, **65**, 781-785.
52. C. J. Calzado, C. Angeli, D. Taratiel, R. Caballol and J.-P. Malrieu, *J. Chem. Phys.*, 2009, **131**, 044327.
53. F. Neese, *Coordination Chemistry Reviews*, 2009, **253**, 526.
54. V. G. Chilkuri, S. DeBeer and F. Neese, *Inorganic Chemistry*, 2020, **59**, 984-995.
55. N. Spiller, V. G. Chilkuri, S. DeBeer and F. Neese, *European Journal of Inorganic Chemistry*, 2020, **2020**, 1525-1538.
56. F. Neese, *J. Phys. Chem. Solids*, 2004, **65**, 781.
57. F. Neese, *J. Biol. Inorg. Chem.*, 2006, **11**, 702.
58. M. Orio, D. A. Pantazis and F. Neese, *Photosynth. Res.*, 2009.
59. M. Orio, D. A. Pantazis, T. Petrenko and F. Neese, *Inorganic Chemistry*, 2009, **48**, 7251-7260.
60. D. A. Pantazis, V. Krewald, M. Orio and F. Neese, *Dalton Transactions*, 2010, **39**, 4959-4967.
61. L. Noodleman, *J. Chem. Phys.*, 1981, **74**, 5737.
62. L. Noodleman and D. A. Case, *Adv. Inorg. Chem.*, 1992, **38**, 423.
63. L. Noodleman and E. R. Davidson, *Chem. Phys.*, 1986, **109**, 131.
64. E. Ruiz, *Struct. Bonding (Berlin)*, 2004, **113**, 91.
65. E. Ruiz, J. Cano, S. Alvarez and P. Alemany, *J. Comput. Chem.*, 1999, **20**, 1391.
66. A. Bencini and F. Totti, *Journal of Chemical Theory and Computation*, 2008, **5**, 144-154.
67. K. Yamaguchi, Y. Takahara, T. Fueno, V. H. Smith, H. F. Schaefer and K. Morokuma, *Applied Quantum Chemistry*1986.

68. S. Yamanaka, T. Kawakami, H. Nagao and K. Yamaguchi, *Chem. Phys. Lett.*, 1994, **231**, 25.
69. A. Bencini and D. Gatteschi, *Journal of the American Chemical Society*, 1986, **108**, 5763-5771.